The Astrophysical Journal Supplement Series, 203:31 (17pp), 2012 December doi:10.1088/0067-0049/203/2/31

CHANDRA OBSERVATIONS OF 3C RADIO SOURCES WITH $z < 0.3$. II. COMPLETING THE SNAPSHOT SURVEY

F. Massaro[1], G. R. Tremblay[2], D. E. Harris[3], P. Kharb[4], D. Axon[4,5,15], B. Balmaverde[6], S. A. Baum[7,8], A. Capetti[6], M. Chiaberge[9,10,11], R. Gilli[12], G. Giovannini[11,12], P. Grandi[13], F. D. Macchetto[9], C. P. O'Dea[3,4], G. Risaliti[14], W. Sparks[9], and E. Torresi[13]

[1] SLAC National Laboratory and Kavli Institute for Particle Astrophysics and Cosmology, 2575 Sand Hill Road, Menlo Park, CA 94025, USA
[2] European Southern Observatory, Karl-Schwarzschild-Str. 2, D-85748 Garching bei Muenchen, Germany
[3] Smithsonian Astrophysical Observatory, 60 Garden Street, Cambridge, MA 02138, USA
[4] Department of Physics, Rochester Institute of Technology, Carlson Center for Imaging Science 76-3144, 84 Lomb Memorial Dr., Rochester, NY 14623, USA
[5] School of Mathematical and Physical Sciences, University of Sussex, Brighton BN1 9QH, UK
[6] INAF-Osservatorio Astrofisico di Torino, Strada Osservatorio 20, I-10025 Pino Torinese, Italy
[7] Carlson Center for Imaging Science 76-3144, 84 Lomb Memorial Dr., Rochester, NY 14623, USA
[8] Radcliffe Institute for Advanced Study, 10 Garden St. Cambridge, MA 02138, USA
[9] Space Telescope Science Institute, 3700 San Martine Drive, Baltimore, MD 21218, USA
[10] Center for Astrophysical Sciences, Johns Hopkins University, 3400 N. Charles Street Baltimore, MD 21218, USA
[11] INAF-Istituto di Radioastronomia di Bologna, Via Gobetti 101, I-40129 Bologna, Italy
[12] INAF-Osservatorio Astronomico di Bologna, Via Ranzani 1, I-40127 Bologna, Italy
[13] INAF-IASF-Istituto di Astrofisica Spaziale e fisica Cosmica di Bologna, Via P. Gobetti 101, I-40129 Bologna, Italy
[14] INAF-Osservatorio Astronomico di Arcetri, Largo E. Fermi 5, I-50125 Firenze, Italy
Received 2012 July 7; accepted 2012 October 16; published 2012 November 28

ABSTRACT

We report on the second round of *Chandra* observations of the 3C snapshot survey developed to observe the complete sample of 3C radio sources with $z < 0.3$ for 8 ks each. In the first paper, we illustrated the basic data reduction and analysis procedures performed for the 30 sources of the 3C sample observed during *Chandra* Cycle 9, while here we present the data for the remaining 27 sources observed during Cycle 12. We measured the X-ray intensity of the nuclei and of any radio hot spots and jet features with associated X-ray emission. X-ray fluxes in three energy bands, i.e., soft, medium, and hard, for all the sources analyzed are also reported. For the stronger nuclei, we also applied the standard spectral analysis, which provides the best-fit values of the X-ray spectral index and absorbing column density. In addition, a detailed analysis of bright X-ray nuclei that could be affected by pile-up has been performed. X-ray emission was detected for all the nuclei of the radio sources in our sample except for 3C 319. Among the current sample, there are two compact steep spectrum radio sources, two broad-line radio galaxies, and one wide angle tail radio galaxy, 3C 89, hosted in a cluster of galaxies clearly visible in our *Chandra* snapshot observation. In addition, we also detected soft X-ray emission arising from the galaxy cluster surrounding 3C 196.1. Finally, X-ray emission from hot spots has been found in three FR II radio sources and, in the case of 3C 459, we also report the detection of X-ray emission associated with the eastern radio lobe as well as X-ray emission cospatial with radio jets in 3C 29 and 3C 402.

Key words: galaxies: active – radio continuum: galaxies – X-rays: general

Online-only material: color figures

1. INTRODUCTION

In recent years, several photometric and spectroscopic snapshot surveys of 3C radio galaxies have been carried out using the *Hubble Space Telescope* (*HST*), approaching the statistical completeness of the radio catalog. A ground-based spectroscopic survey for the whole sample with the Galileo telescope has been completed (Buttiglione et al. 2009) and deep ground-based infrared images are also available in the *K* band. Radio images with arcsecond resolution for the majority of the 3C sources are available from the NRAO VLA Archive Survey (NVAS) and in the archives of the Very Large Array (VLA) and MERLIN observatories. A few radio maps were made available to us by our colleagues. Finally, VLBA data for several of the 3C objects with $z < 0.2$ have already been obtained (see, e.g., Giovannini et al. 2001; Liuzzo et al. 2009, and references therein).

To extend the wavelength coverage, we embarked on a 3C snapshot survey in the X-ray with *Chandra*, the only X-ray facility with angular resolution comparable to that at optical and radio frequencies. Previous X-ray studies were mostly based on samples of X-ray-bright sources or objects with well-known peculiarities instead of carefully selected and complete samples, unbiased with respect to orientation and spectroscopic classification like the 3C catalog. However, 56 sources in the 3C sample (Mackay 1971; Spinrad et al. 1985) at $z < 0.3$ remained unobserved by *Chandra* before Cycle 9, when we started our snapshot survey. In our first paper (Massaro et al. 2010), we reported the data reduction and analysis procedures used to study the first 30 radio sources, while in this work we present a similar investigation of the remaining 27 sources to complete the sample at $z < 0.3$.[16]

The main aims of our snapshot survey are to detect X-ray emission from jets and hot spots, to eventually determine their X-ray emission processes on a firm statistical basis, and to study the nuclear emission of the host galaxy. We also want to obtain

[15] Deceased.

[16] This new sample includes 3C 346 that have been re-observed in Cycle 12 because during Cycle 9 its *Chandra* observation was affected by high background (see Massaro et al. 2010 for more details).

Table 1
Source List of the Chandra AO12 Snapshot Survey of 3C Radio Sources with $z < 0.3$

3C	Class[a]	R.A. (J2000) (hh mm ss)	Decl. (J2000) (dd mm ss)	z[b]	D_L (Mpc)	Scale (kpc arcsec^{-1})	$N_{H,Gal}$[c] (cm^{-2})	m_v[d]	S_{178}[e] (Jy)	*Chandra* Obs ID	Obs. Date (yyyy-mm-dd)
29	FR I–LEG	00 57 34.895	−01 23 27.37	0.0448	193.1	0.858	3.66e20	14.1	15.1	12721	2011-05-23
63	FR II–HEG	02 20 54.316	−01 56 50.72	0.175	824.7	2.896	2.47e20	18.5	19.2	12722	2010-10-27
79	FR II–HEG	03 10 00.090	+17 05 58.52	0.2559	1265.3	3.889	8.72e20	18.5	30.5	12723	2010-11-01
89	WAT – ?	03 34 15.574	−01 10 56.09	0.1386	638.1	2.386	7.02e20	16.0	20.2	12724	2010-11-03
93.1	CSS–HEG	03 48 46.934	+33 53 15.28	0.2430	1192.7	3.743	1.15e21	19.0	9.9	12725	2010-11-04
130	FR I – ?	04 52 52.836	+52 04 47.09	0.1090	491.9	1.939	3.66e21	16.5	15.5	12726	2010-12-11
166	FR II–LEG	06 45 24.098	+21 21 51.30	0.2449	1203.3	3.764	1.71e21	19.5	14.7	12727	2010-11-29
180	FR II–HEG	07 27 04.880	−02 04 30.33	0.22	1065.5	3.471	1.36e21	19.0	15.1	12728	2010-12-24
196.1	FR II–LEG	08 15 28.10	−03 08 28.00	0.198	946.4	3.197	5.82e20	17.5	18.6	12729	2011-02-11
198	FR II – NLRG	08 22 31.80	+05 57 07.90	0.0815	360.8	1.496	2.24e20	16.8	9.7	12730	2011-01-07
223	FR II–HEG	09 39 52.755	+35 53 58.86	0.1368	629.0	2.360	1.04e20	17.1	14.7	12731	2012-01-07
234	FR II–HEG	10 01 49.526	+28 47 08.87	0.1848	876.2	3.026	1.76e20	17.3	31.4	12732	2011-01-19
258	CSS – ?	11 24 43.881	+19 19 29.50	0.165?	772.7	2.760	1.51e20	19.5	9.7	12733	2010-11-01
284	FR II–HEG	13 11 04.666	+27 28 07.15	0.2394	1172.6	3.701	9.75e19	18.0	11.3	12735	2010-11-17
314.1	FR I–LEG	15 10 27.064	+70 46 07.37	0.1197	544.2	2.104	1.93e20	17.0	10.6	12736	2012-01-02
319	FR II – ?	15 24 05.640	+54 28 18.40	0.192	914.3	3.120	1.16e20	17.0	10.6	12736	2010-10-25
357	FR II–LEG	17 28 20.109	+31 46 02.58	0.1662	778.9	2.776	3.07e20	15.5	9.7	12738	2010-10-31
379.1	FR II–HEG	18 24 32.976	+74 20 59.00	0.256	1265.8	3.890	5.43e20	18.0	7.4	12739	2011-04-04
402	FR I – NLRG	19 41 45.899	+50 35 45.86	0.0239	101.4	0.469	1.07e21	14.0	10.1	12740	2011-07-12
403.1	FR II–LEG	19 52 30.50	−01 17 18.00	0.0554	240.7	1.048	1.19e21	16.0	13.5	12741	2010-11-27
410	FR II–BLO	20 20 06.60	+29 42 14.20	0.2485	1223.5	3.805	4.35e21	19.5	34.6	12742	2011-09-24
424	FR I–LEG	20 48 12.087	+07 01 17.17	0.127	580.2	2.215	7.05e20	18.0	14.6	12743	2011-04-15
430	FR II–LEG	21 18 19.094	+60 48 07.77	0.0541	234.8	1.025	3.31e21	15.0	33.7	12744	2011-11-14
436	FR II–HEG	21 44 11.727	+28 10 18.92	0.2145	1035.5	3.403	6.43e20	18.2	17.8	12745	2011-05-27
456	FR II–HEG	23 12 28.076	+09 19 26.39	0.2330	1137.0	3.626	3.70e20	18.5	10.6	12746	2011-01-17
458	FR II–HEG	23 12 52.083	+05 16 49.77	0.289	1455.2	4.246	5.85e20	20.0	14.5	12747	2010-10-10
459	FR II–BLO	23 16 35.30	+04 05 18.30	0.2199	1064.9	3.469	5.24e20	17.6	25.6	12734	2011-10-13

Notes.
[a] The "class" column contains both a radio descriptor (Fanaroff–Riley class I or II), compact steep spectrum (CSS), wide angle tail (WAT) radio galaxy and the optical spectroscopic designation, "low excitation galaxy (LEG)," "high excitation galaxy (HEG)," "broad-line object (BLO)," and "narrow-line radio galaxy (NRLG)." The symbol "?" indicates those optical classifications that are uncertain or not reported in the literature.
[b] Redshift measurements are taken form Chiaberge et al. (2002), Floyd et al. (2008), and Buttiglione et al. (2009).
[c] Galactic neutral hydrogen column densities $N_{H,Gal}$ are taken form Kalberla et al. (2005).
[d] m_v is the visual magnitude (Spinrad et al. 1985).
[e] S_{178} is the flux density at 178 MHz, taken from Spinrad et al. (1985).

the spectral energy distribution of an unbiased sample of nuclear and non-nuclear features. In a future paper, the resulting data set will be used to test the Fanaroff–Riley dichotomy in terms of differences in the nature of nuclear absorption in FR I and FR II sources. However, it is first necessary to obtain the basic source parameters for the newly acquired data, so this paper consists of these data for the remaining 3C radio galaxies at $z < 0.3$.

The paper is organized as follows: A brief description of the observations and data reduction procedures is given is Section 2; the general and particular (i.e., single source) results are described in Section 3. The conclusions and a short summary are given in Section 4.

For our numerical results, we use cgs units unless stated otherwise and we assume a flat cosmology with $H_0 = 72$ km s^{-1} Mpc^{-1}, $\Omega_M = 0.27$, and $\Omega_\Lambda = 0.73$ (Dunkley et al. 2009). Spectral indices, α, are defined by flux density, $S_\nu \propto \nu^{-\alpha}$.

2. OBSERVATIONS, DATA REDUCTION, AND BASIC PARAMETERS

Our data reduction and data analysis procedures are described in Massaro et al. (2009a, 2010), and here we provide only an overview.

The sources observed in this project are listed in Table 1 together with their salient parameters. Each was observed for a nominal 8 ks, and the actual live times are given in Table 2, together with the nuclear fluxes. We used the ACIS-S back-illuminated chip in very faint mode with standard frame times (3.2 s). All the observations had four chips turned on: I2, I3, S2, and S3. The data reduction has been performed following the standard reduction procedure described in the Chandra Interactive Analysis of Observations (CIAO) threads,[17] using CIAO v4.4 and the Chandra Calibration Database version 4.4.8. Level 2 event files were generated using the *acis_process_events* task. Events were filtered for grades 0, 2, 3, 4, and 6. Light curves for every data set were extracted and checked for high background intervals; none were found.

Astrometric registration was achieved by changing the appropriate keywords in the fits header so as to align the nuclear X-ray position with that of the radio. The celestial coordinates of the X-ray nuclei were measured on displays of the event file which were regridded to a pixel size of 0.″0615, energy filtered for 0.5–7 keV, and smoothed with a Gaussian of FWHM = 0.″35 or less. A similar measurement was made on the radio image and the difference in each coordinate provided the amount of the required shift. In most cases, the total shift ($\sqrt{\Delta(\mathrm{R.A.})^2 + \Delta(\mathrm{Decl.})^2}$ was of the order of 0.″4 or less.

[17] http://cxc.harvard.edu/ciao/guides/index.html

Table 2
Nuclear X-Ray Fluxes in Units of 10^{-15} erg cm^{-2} s^{-1}

3C	LivTim[a] (ks)	Net[b] (counts)	Ext. Ratio[c]	f(Soft) (0.5–1 keV)	f(Medium) (1–2 keV)	f(Hard) (2–7 keV)	f(Total) (0.5–7 keV)	HR	$N_{\rm H}(z)$[d] (10^{22} cm^{-2})	L_X (10^{42} erg s^{-1})
29	7.95	51(7)	0.52(0.11)	2.9(1.1)	11.9(2.3)	29.1(6.7)	43.9(7.2)	0.42(0.19)	<1.81	0.19(0.03)
63	7.95	513(22)	0.91(0.06)	9.0(2.1)	101(7)	496(30)	606(31)	0.66(0.06)	2.19–5.18	49.3(2.5)
79	7.69	104(10)	0.91(0.13)	3.4(1.2)	3.7(1.3)	200(21)	207(21)	0.96(0.15)	5.24–24.5	39.7(4.1)
93.1	7.69	101(10)	0.97(0.13)	10.0(2.3)	18.6(2.8)	56.1(9.2)	98.7(9.9)	0.50(0.14)	1.09–4.85	14.4(1.7)
130	7.95	28(5)	0.54(0.20)	2.4(1.1)	7.2(1.9)	12.7(4.8)	22.3(5.3)	0.28(0.27)	<3.27	0.64(0.15)
166	7.95	432(20)	0.96(0.06)	37.3(4.2)	94.4(6.5)	238(20)	370(22)	0.43(0.07)	1.07–3.63	64.0(3.7)
180	7.95	26(5)	0.93(0.27)	1.90(0.85)	2.1(1.0)	40.3(9.8)	44.3(9.9)	0.90(0.31)	2.35–24.5	6.0(1.3)
198	7.95	5(2)	0.83(0.57)	···	0.74(0.53)	···	0.74(0.53)	···	···	0.04(0.02)
223	7.95	113(11)	0.95(0.13)	5.9(1.6)	15.6(2.7)	130(16)	151(16)	0.79(0.14)	2.34–8.79	7.17(0.78)
234	7.95	311(17)	0.95(0.07)	135(19)	81(11)	433(31)	649(37)	0.69(0.08)	2.24–5.74	59.9(3.5)
258	7.95	6(2)	0.85(0.99)	···	1.40(0.81)	5.4(3.9)	7.3(4.0)	0.68(0.52)	<24.4	0.52(0.29)
284	7.95	16(4)	1.00(0.40)	2.6(1.1)	3.0(1.1)	5.4(3.1)	11.1(3.5)	0.29(0.41)	<3.29	1.83(0.58)
314.1	7.95	14(4)	1.00(0.40)	1.81(0.91)	3.1(1.1)	6.1(3.6)	11.0(3.9)	0.33(0.43)	<5.11	0.39(0.14)
357	7.95	129(11)	0.95(0.12)	2.5(1.0)	18.4(3.0)	145(16)	166(16)	0.77(0.13)	2.45–8.68	12.0(1.2)
379.1	7.95	30(5)	0.97(0.25)	···	2.01(0.90)	54(11)	56(11)	0.93(0.27)	3.25–24.5	10.8(2.1)
402	7.95	167(13)	0.83(0.09)	21.7(3.1)	35.9(3.9)	55.2(9.1)	113(10)	0.21(0.11)	<1.00	0.14(0.01)
403.1	7.95	6(2)	1.00(0.74)	···	1.25(0.72)	2.5(1.8)	4.3(2.0)	0.33(0.53)	<6.70	0.03(0.01)
410	7.95	1122(34)	0.89(0.04)	24.6(3.5)	193(10)	1220(47)	1437(48)	0.73(0.04)	3.23–6.41	257(9)
424	7.95	52(7)	0.67(0.13)	1.24(0.89)	9.5(2.2)	58(10)	68(10)	0.72(0.19)	1.56–8.03	2.76(0.42)
430	7.95	8(3)	0.62(0.41)	···	1.23(0.71)	10.6(4.7)	11.8(4.8)	0.79(0.52)	<24.1	0.08(0.03)
436	7.95	39(6)	0.76(0.18)	1.00(0.58)	0.91(0.64)	80(14)	81(14)	0.98(0.24)	3.75–24.5	10.5(1.8)
456	7.95	328(18)	0.92(0.07)	3.1(1.2)	15.9(2.8)	545(32)	564(32)	0.94(0.08)	5.24–24.4	87.2(5.0)
458	7.95	37(6)	1.00(0.25)	···	2.15(0.97)	72(13)	74(13)	0.94(0.24)	3.67–24.5	18.7(3.2)
459	7.95	100(10)	0.87(0.12)	13.8(2.4)	16.7(2.7)	58(10)	88(11)	0.55(0.16)	1.18–5.63	12.0(1.5)

Notes. Values in parentheses are 1σ uncertainties.
[a] LivTim is the live time.
[b] Net is the net counts within a circle of radius $= 2''$.
[c] Ext. Ratio ("Extent Ratio") is the ratio of the net counts in the $r = 2''$ circle to the net counts in the $r = 10''$ circle. Values significantly less than 0.9 indicate the presence of extended emission around the nuclear component. A more detailed analysis of the radio sources with extended emission around their nuclei will be presented in Balmaverde et al. (2012).
[d] As per the discussion in the text, we calculate the value of $N_{\rm H}(z)$ required to produce the observed HR values. The uncertainty given here is indicative only: it is the range of $N_{\rm H}(z)$ covered by the uncertainty in the HR and allowing α_X to range from 0.5 to 1.5. Obviously there may be some sources with intrinsic spectral indices outside of this range.

2.1. Fluxmaps

We created three different fluxmaps (soft, medium, and hard, in the ranges 0.5–1, 1–2, 2–7 keV, respectively) by filtering the event file with the appropriate energy range and dividing the data with monochromatic exposure maps (with nominal energies of soft = 0.8 keV, medium = 1.4 keV, and hard = 4 keV). The exposure maps and the fluxmaps were regridded to a common pixel size which was usually one-fourth the size of a native ACIS pixel (native = 0.″492). In fact, to achieve the angular resolution of the *Chandra* mirrors, we need to avoid the undersampling imposed by the ACIS pixel size. Since the location of each event is a real number and not an integer value denoting only the center of a pixel location, and since *Chandra* routinely dithers on the sky, avoiding undersampling can be achieved by regridding to obtain pixel sizes of 0.″123 or smaller. For sources of large angular extent we used 1/2 or no regridding.

To obtain maps with brightness units of erg cm^{-2} s^{-1} pixel^{-1}, we multiplied each event by the nominal energy of its respective band (see also Massaro et al. 2009b).

To measure observed fluxes for any feature, we construct an appropriate region (usually circular) and two adjacent background regions of the same size. The two background regions were chosen so as to avoid contaminating X-ray emission (and also radio emission) and permitted us to sample both sides of the jet features and two areas close to hot spots, and avoid contamination from weak emission surrounding the nuclei of the galaxies (e.g., Massaro et al. 2011).

The total energy in any particular band for any particular region is measured with funtools,[18] and since our procedure for making fluxmaps includes multiplying each event by the nominal energy ($h * \upsilon_{\rm nominal}$ ergs), the resulting measurement is in cgs units. The actual energy in the band is the sum of all events within the region, each with its observed energy. By applying a correction factor of $E(average)/E(nominal)$, we recover the actual total energy for that particular region since to derive E(average) the actual E values are used. This correction ranged from a few to 15%. A 1σ error is assigned based on the usual $\sqrt{\text{number-of-counts}}$ in the on and background regions. Fluxes for the nuclei are given in Table 2.

2.2. X-Ray Spectral Analysis of the Stronger Nuclei

We have performed an X-ray spectral analysis for those nuclear point sources containing 250 or more counts, so as to quantify their X-ray spectral indices α_X, the presence or absence of significant intrinsic absorption $N_H(z)$, and the role played by mild pile-up in artificially hardening the spectrum.

The spectral data were extracted from a 1.″5 aperture using the CIAO 4.4 routine `specextract`, thereby automating the

[18] http://www.cfa.harvard.edu/~john/funtools

Table 3
Estimates of Intrinsic N_H for the AO9 Sources that Are Not Affected by Pile-up

3C	Redshift	HR	N_H (10^{22} cm^{-2})
20	0.174	0.99(0.12)	5.42–24.4
52	0.2854	0.86(0.47)	1.29–24.5
61.1	0.1878	0.84(0.21)	2.39–24.4
76.1	0.0324	0.78(0.29)	1.13–21.5
105	0.089	0.98(0.08)	3.03–23.6
132	0.214	0.94(0.21)	3.49–24.5
135	0.1273	0.80(0.26)	1.63–24.2
165	0.2957	0.79(0.24)	2.27–24.5
171	0.2384	0.96(0.11)	5.82–24.5
213.1	0.1937	0.22(0.19)	<2.82
223.1	0.1075	0.97(0.14)	4.00–24.2
293	0.045	0.97(0.10)	3.80–21.5
300	0.27	0.37(0.12)	<3.92
303.1	0.267	0.68(0.47)	<24.5
305	0.0416	0.14(0.22)	<1.76
315	0.1083	1.00(0.71)	<24.2
349	0.205	0.68(0.09)	2.32–6.57
381	0.1605	0.96(0.09)	5.14–24.4
436	0.2145	0.94(0.23)	2.25–24.5
460	0.268	0.88(0.24)	2.93–24.5

Notes. Values in parentheses are 1σ uncertainties. As for Table 2, we calculate the value of N_H required to produce the observed HR values. The uncertainty given here is indicative only: it is the range of N_H covered by the uncertainty in the HR and allowing α_X to range from 0.5 to 1.5 (see Section 3.2 for more details).

creation of count-weighted response matrices. The background-subtracted spectra were then filtered in energy between 0.3 and 7 keV, binned using a 30 count threshold, and fit with absorbed power-law models using iterative χ^2 minimization techniques with XSPEC version 12.6 (Arnaud 1996).

Two multiplicative models are fit to each source: (1) a simple redshifted power law with Galactic and intrinsic photoelectric absorption components (`phabs×zphabs×zpowerlaw` in XSPEC syntax) and (2) the same model with an additional pile-up component (`pileup×phabs×zphabs×zpowerlaw`), using the XSPEC implementation of the *Chandra* pile-up model described by Davis (2001).

Prior to fitting, the Milky Way hydrogen column density and the source redshift were fixed. The two main variable parameters, namely, the intrinsic absorption $N_H(z)$ and X-ray photon index Γ (i.e., $\Gamma = \alpha_X + 1$) were allowed to vary in a first pass fit, but subsequently stepped through a range of possible physical values to explore the parameter space, determine 90% confidence intervals, and quantify the degree to which $N_H(z)$ and Γ are degenerate.

Monte Carlo Markov Chains were created to further aid our understanding of these behaviors. We have also explored the possible effect of pile-up on our sources, which we discuss in the section below.

We also note that those sources with inverted best-fit spectral indices ($\Gamma < 1$ or $\alpha_X < 0$) are likely to be unphysical for the power-law-plus-absorption model. Inverted spectra for the energy band 0.5–7 keV can result from Compton thick models. 3C 79, 3C 105, 3C 234, and 3C 332 are not included in this analysis as no constraints can be found using an absorbed power-law model. A detailed analysis of the X-ray spectrum of 3C 234 can be found in Piconcelli et al. (2008) while the X-ray spectrum of 3C 105 is presented in Massaro et al. (2010).

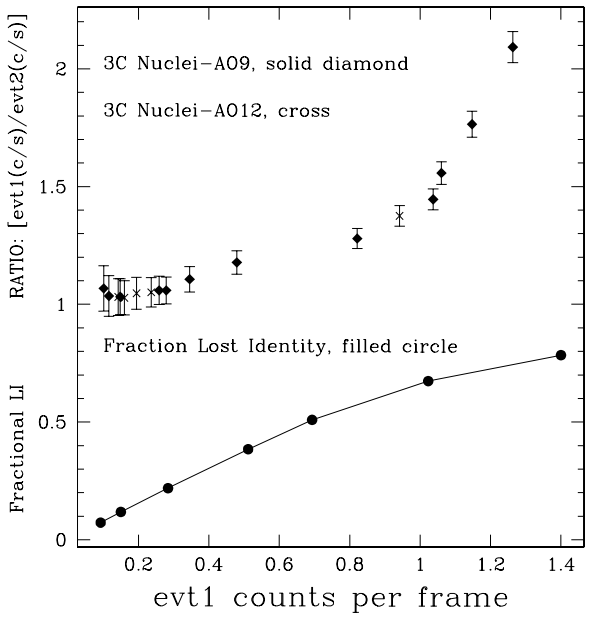

Figure 1. As a function of the total event 1 count rate (counts per frame) we show the ratio of evt1 count rate to evt2 count rate for the brighter nuclei from the *Chandra* 3C snapshot survey. These data are the values $\geqslant 1$ (with 1σ statistical error bars). The plotted values below 1 are the calculated fractions of incoming photons which lose their identity by ending up in piled events.

Those sources whose count rates proved insufficient for χ^2 minimization techniques were instead fit using Cash (1979) statistics. Spectral information was also obtained using hardness ratios (see also Table 3 and Figure 2 for more details). Then the results of our spectral analysis are presented in Table 4.

2.3. The Effects of Mild Pile-up

In our previous data paper on the AO9 sample of 3C sources (Massaro et al. 2010), we erroneously neglected the effects of mild pile-up in the ACIS CCDs (but see the note added in proof, Massaro et al. 2010). In this section, we describe our diagnostic for pile-up and suggest a threshold count rate, above which spectral analysis and our use of hardness ratios to estimate the excess absorption (the column density of N_H ascribed to material at the source) are suspect. The application of the "jdpileup model" in Sherpa[19] (Freeman et al. 2001) and in XSPEC (Arnaud 1996) for our data is discussed in Section 2.2.

As described in Section 3.2 of Harris et al. (2011), we have verified that the standard grade filtering that is applied to all ACIS data in pipeline processing means that a fraction of piled events are rejected in passing from the event 1 files to event 2. This is caused by "grade migration," an inevitable consequence of pile-up (Davis 2001). Thus, we choose the ratio of count rates (evt1/evt2) as a robust diagnostic of pile-up. In Figure 1, we demonstrate this for our sources by plotting the ratio against the event 1 counts per frame. We have also checked weaker sources and verified that their evt1 and evt2 count rates are equal within the errors.

We have used PIMMS to elucidate what this means in terms of pile-up fraction. While PIMMS does not accommodate grade migration, by using the evt1 count rate, we are able to derive all necessary quantities. For a series of input counts s^{-1} to PIMMS, with a power-law spectrum of $\alpha_X = 1$ and no absorption, PIMMS returns the fractional count rate, Fp, which is the

[19] http://cxc.harvard.edu/sherpa/

Table 4
Spectral Analysis of the Brighter Nuclei

Source (1)	z (2)	FR/Opt. Class (3)	$N_{H,Gal}$ ($\times 10^{20}$ cm^{-2}) (4)	Γ (5)	$N_H(z)$ ($\times 10^{20}$ cm^{-2}) (6)	Pile-up G.M. (%) (7)	χ^2/dof (8)
3C 17*	0.2197	II/BLO	2.86	$1.75^{+0.12}_{-0.11}$	$[0.0]^{+3.4}_{\downarrow}$	(0.94†)	22.6/31
3C 18*	0.188	II/BLO	5.33	$1.12^{+0.17}_{-0.11}$	$[0.0]^{+9.0}_{\downarrow}$	(1.0†)	40.6/28
3C 33.1*	0.181	II/BLO	20.0	1.47 ± 0.2	469 ± 135	(1.0)	19.3/18
3C 63	0.175	II/HEG	2.47	(1.36†)	$71.0^{+28.0}_{-26.0}$	(1.0†)	3.6/13
3C 133*	0.278	II/HEG	25.4	2.63 ± 0.2	116 ± 45	(1.0)	18.3/15
3C 166	0.245	II/LEG	17.1	$1.65^{+0.27}_{-0.22}$	$[0.0]^{+12.3}_{\downarrow}$	(1.0)	9.41/9
3C 184.1*	0.118	II/BLO	3.15	1.80 ± 0.5	358 ± 165	(1.0)	12/13
3C 197.1*	0.130	II/BLO	4.20	1.64 ± 0.13	$[0.0]^{+7.4}_{\downarrow}$	(1.0)	24.5/24
3C 287.1*	0.2156	II/BLO	1.63	$1.43^{+0.10}_{-0.10}$	$[0.0]^{\uparrow}_{\downarrow}$	(1.0†)	24.6/32
3C 323.1*	0.2643	II/BLO	3.79	$0.406^{+0.15}_{-0.15}$	$[0.0]^{\uparrow}_{\downarrow}$	(1.0)	16.6/13
3C 410	0.249	II/BLO	43.5	(1.78†)	$66.7^{+21.0}_{-19.1}$	(1.0)	30.5/32
3C 456	0.233	II/HEG	3.70	(1.89†)	867.9^{+174}_{-150}	(1.0†)	3.8/7

Notes. The model used for the data fitting procedure is `pileup` × `phabs` × `zphabs` × `zpowerlaw` in XSPEC syntax. The number of counts per bin is shown in parentheses. Spectra with 30 count bins. For these fits, we show in square brackets the corresponding range of best-fit N_H as the photon index Γ is stepped through values of 1.0 to 3.0. Column 1: source name (an asterisk indicates an AO09 source adversely affected by pile-up, warranting a re-analysis). Column 2: source redshift (this parameter was fixed in all spectral fits). Column 3: Fanaroff–Riley radio classification (Fanaroff & Riley 1974) and optical emission line classification (HEG: "high excitation galaxy"; LEG: "low excitation galaxy"; BLO: "broad-line object," classifications, Buttiglione et al. 2009). Column 4: Galactic absorption column density in units of $\times 10^{20}$ cm^{-2} (Kalberla et al. 2005; this parameter was fixed in all spectral fits). Column 5: photon index (note that $\alpha_X = \Gamma - 1$. A common value for unabsorbed AGN is $\Gamma = 1.9$ or $\alpha_X = 0.9$.). Column 6: intrinsic absorbing column density in units of 10^{20} cm^{-2}. Parentheses "()" indicate that the value was fixed for the listed fit. A dagger symbol means that the parameter was initially left free in a first-pass fit, then subsequently fixed at its original best-fit value. A bracket around a number means that the parameter was not constrained. We also show a number in brackets with an upper limit listed. A down arrow indicates that no lower bound is found. A bracketed range (e.g., [1.0 → 3.0]) indicates that a series of fits were computed using a grid of values ranging between the limits listed in brackets. For the column density $N_H(z)$, we list the corresponding best-fit values as we step through this range of Γ. Column 7: grade migration parameter from `jdpileup`. Column 8: χ^2/degrees of freedom.

fraction of piled events to total (i.e., evt1) events. The "output" count rate of PIMMS is the rate of unpiled events. Thus, the total count rate (our observed evt1 counts s^{-1}) is given by

$$\mathrm{evt1(counts\,s^{-1})} = \frac{\mathrm{out(counts\,s^{-1})}}{(1 - Fp)}. \quad (1)$$

In judging "how bad things can get," we prefer a new parameter, "$F_{\rm li}$," rather than the reported fraction of piled to total events. We define $F_{\rm li}$ as the fraction of incoming *photons* which lose their identity to the total number of incoming photons. So $F_{\rm li}$ tells us what fraction of the total photons end up in piled events:

$$F_{\rm li} = \frac{\mathrm{IN} - \mathrm{OUT}}{\mathrm{IN}}, \quad (2)$$

where IN is the input counts s^{-1} to PIMMS and OUT is the count rate PIMMS reports, i.e., the unpiled rate. $F_{\rm li}$ is plotted in Figure 1.

The obvious question then is; As counts frame^{-1} increase, when would we start getting significantly wrong spectral parameters from Sherpa? The answer to this question is not unique: it depends on the spectral distribution of the source and on the accuracy of our estimates of spectral parameters (and hence on the number of events available for spectral analysis). For our purposes, we subjectively assign 0.2 counts frame^{-1} (where more than 10% of incoming photons end up in piled events) as the threshold above which we should be circumspect of spectral parameters. For our data with 3.2 s frame time and an exposure time of 8 ks, this corresponds to 0.06 counts s^{-1} and 480 total counts. This criterion applies to one source in the AO12 sample and nine from the AO9 sample.

3. RESULTS

3.1. General

X-ray emission was detected for all the nuclei in the sample except for 3C 319, an FR II radio galaxy of small angular size. The observed nuclear fluxes are presented in Table 2 in the soft, medium, and hard bands together with the X-ray luminosity and the X-ray hardness ratio HR (e.g., Massaro et al. 2010, 2011). This has been evaluated according to the simple relation: $(H-M)/(H+M)$, where H and M are the X-ray fluxes in the hard and the medium bands, respectively. In Table 2, the uncertainties on the observed values of HR have been derived from the errors on the flux values. The HR values have not been computed using the soft band because it is the band most affected by absorption. Thus, for large column densities, there are very few counts (or none) in the soft band. Values of HR are not provided for 3C 319 (no detection of nucleus) and the two sources, 3C89 and 3C196.1, which lie in clusters of galaxies, making it difficult to separate nuclear emission from the relatively bright X-ray emission from the cluster gas.

In addition, as performed for the previous subset of 3C sources observed during *Chandra* Cycle 9, we measured the net number of counts within circular regions of radii 2″ and 10″, both centered on the nucleus of each source. In Table 2, we give the $r = 2''$ result together with the ratio of $r2/r10$, a diagnostic for the presence of extended emission around the nucleus. The only exceptions are 3C 89 and 3C 196.1 which lie in X-ray-detected galaxy clusters, as shown in Figures 3–6, as well as 3C 319 which is undetected. This ratio should be close to unity for an unresolved source: the on-axis encircled energy for $r = 2''$ is

Table 5
Radio Components with X-Ray Detections

3C	Component[a]	Radius[b] (arcsec)	Counts (bkg)[c]	Detection Significance[d]	$f_{0.5-1keV}$ (cgs)	$f_{1-2\,keV}$ (cgs)	$f_{2-7\,keV}$ (cgs)	$f_{0.5-7\,keV}$ (cgs)	L_X (10^{41} erg s^{-1})
29	*k* - s 2.7	1.0	8(1)	4.7σ	1.39(0.80)	1.67(0.84)	...	3.1(1.2)	0.014(0.005)
234	*h* - w 45	2.0	5(1)	3.2σ	...	0.86(0.62)	3.2(3.1)	4.1(3.3)	0.38(0.30)
402	*k* - s 1.7	0.8	18(7)	3.6σ	4.3(1.9)	1.25(0.86)	1.58(1.54)	7.1(2.6)	0.009(0.003)
436	*h* - s 43	1.5	4(1)	2.7σ	...	0.92(0.65)	...	3.2(2.0)	0.41(0.26)
458	*h* - e 104	2.0	3(1)	2.0σ	...	0.78(0.55)	...	2.2(1.5)	0.57(0.39)
459	*l* - e 1.3	0.8	24(13)	2.9σ	4.2(1.8)	...	...	4.2(1.8)	0.74(0.34)

Notes. Fluxes are given in units of 10^{-15} erg cm^{-2} s^{-1}.
[a] The component designation is comprised of a letter indicating the classification (i.e., knot *k*, hot spot *h*, lobe *l*), a cardinal direction plus the distance from the nucleus in arcseconds (Massaro et al. 2011).
[b] The radius column gives the size of the aperture used for photometry.
[c] The count column gives the total counts in the photometric circle together with the expected background counts in parentheses; both for the 0.5–7 keV band.
[d] The confidence level of each detection evaluated adopting a Poisson distribution.

≈0.97 so we expect only a small increase between $r = 2''$ and $r = 10''$ for an unresolved source.

Among the X-ray-detected sources, we found two compact steep spectrum (CSS) radio sources, 3C 93.1 and 3C 258, two broad-line radio galaxies, 3C 410 and 3C 459, and one wide angle tail (WAT) radio galaxy, 3C 89, hosted in a cluster of galaxies with the largest known X-ray cavity (Sun et al. 2012). In addition, we detected soft X-ray emission arising from the galaxy cluster surrounding the FR II radio galaxy 3C 196.1. For three of our sources, we have hot spot detections in our *Chandra* images, with confidence levels between 2.0σ and 3.2σ. In addition, in the case of 3C 459 we also detect the X-ray emission arising from the eastern radio lobe. Finally, we detected X-ray emission cospatial with radio jets in 3C 29 (see Figure 7) and 3C 402. Fluxes for both jet and hot spot structures found in our sample are reported in Table 5. In the same table, we also provide the confidence level of each detection evaluated adopting a Poisson distribution.

3.2. Incidence of Intrinsic Absorption

As already investigated in Massaro et al. (2010), we performed a photometric analysis to estimate the presence of intrinsic absorption $N_{\rm H}(z)$ in our 3C sample. However, our refined study is based on the values of the hardness ratios HRs (see Section 3.1) derived from the analysis of the nuclear X-ray fluxes rather than on the ratio between the medium and the hard X-ray fluxes as previously performed (Massaro et al. 2010). Our results have also been compared with a detailed spectral analysis that has been performed only for the bright nuclei (see Section 2.2).

Most nuclei of radio galaxies show X-ray spectra well described by a simple power-law model with α_X values ranging between 0.5 and 1.5 or occasionally larger. For those sources with little intrinsic absorbing material (i.e., the galactic $N_{\rm H,Gal}$ values are the major contributors to the total absorption), the expected HR can be computed using the X-ray fluxes in the hard and medium bands.

However, we remark that if a generic source is Compton thick (i.e., $N_{\rm H}(z) > 10^{24}$ cm^{-2}) or if its X-ray spectrum is inverted (i.e., $\alpha_X < 0$) the hardness ratios cannot provide a good estimate of absorption. In particular, for Compton thick sources, even if they are very rare among radio loud active galactic nuclei (AGNs), the spectrum could be dominated by a reflection component providing a low estimate of the intrinsic absorption even if the source is heavily absorbed. This could also occur if the intrinsic spectrum has some features, such as for example emission lines, which only a detailed spectral fitting procedure can reveal providing the correct estimate of $N_{\rm H}(z)$. Thus, values of the intrinsic absorption estimated via photometry (i.e., hardness ratios) could be different with respect to those evaluated from spectral analysis and are thus only indicative of the presence of the absorbing material.

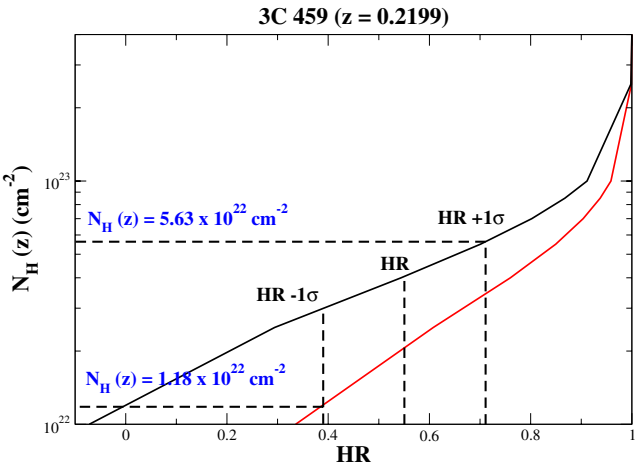

Figure 2. Relation between HR and the intrinsic $N_{\rm H}(z)$ column density resulting from the simulated spectra at redshift 0.2199 as for 3C 459 and computed for the case of $\alpha_X = 0.5$ (black solid line) and 1.5 (red solid line).
(A color version of this figure is available in the online journal.)

On the other hand, due to the relatively short exposure times of our snapshot survey, we often cannot recover the parameters of interest (α_X and $N_{\rm H}(z)$) from the spectral fits but it is possible to derive a range of intrinsic $N_{\rm H}(z)$ column densities corresponding to some chosen range in α_X by using simulated spectra.

We performed numerical simulations with XSPEC deriving the values of $N_{\rm H}(z)$ in the case of an intrinsically absorbed power-law spectrum with different values of the spectral index α_X and source redshift z corresponding to different values of HR. These simulated spectra permit us to derive the relation needed to estimate the intrinsic absorbing column density for an observed value of HR. We iterate this procedure for two values of α_X corresponding to 0.5 and 1.5. We note that in this photometric analysis, we adopted a more restricted energy range of α_X with respect to that used in the X-ray spectral analysis (see Section 2.2) but in agreement with our previous investigation

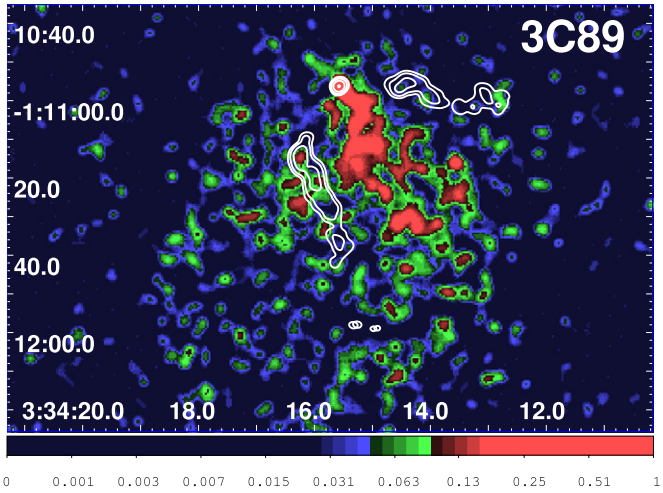

Figure 3. X-ray image of 3C89 for the energy band 0.5–7 keV. The event file has been smoothed with a Gaussian of FWHM = 2.″9. Brightness units are counts per pixel. The pixel size is 0.″492. The radio contours come from a 1.5 GHz map downloaded from the NVAS and start at 0.5 mJy beam^{-1}, increasing by factors of four. The clean beam is 1.″5 × 1.″3 with major axis in P.A. = −57°.

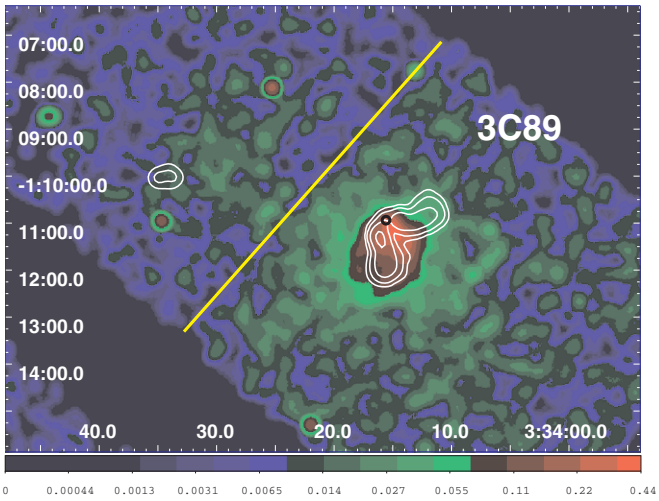

Figure 4. X-ray image of 3C89 at low resolution for the energy band 0.5–7 keV. The event file has been regridded to a pixel size of 0.″984 and smoothed with a Gaussian of FWHM = 10″. Brightness units are counts per pixel. The radio contours come from a 1.5 GHz map downloaded from the NVAS and start at 5 mJy beam^{-1}, increasing by factors of four. The clean beam is 16″ × 13″ with major axis in P.A. = −12°. The small black circle shows the position of the host galaxy and the yellow line follows the edge of the S3 chip.

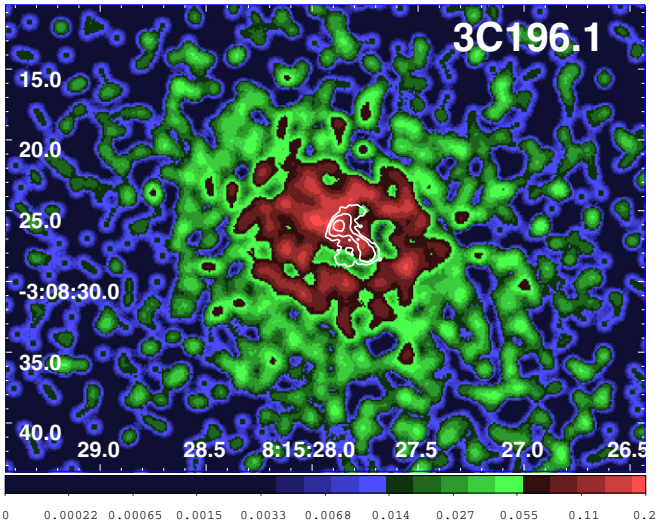

Figure 5. X-ray image of the inner part of the cluster emission from 3C196.1 for the energy band 0.5–7 keV. The event file has been regridded to a pixel size of 0.″123 and smoothed with a Gaussian of FWHM = 1.″0. Brightness units are counts per pixel. The radio contours come from an 8.4 GHz VLA map kindly provided by C. C. Cheung and start at 0.5 mJy beam^{-1}, increasing by factors of four. The clean beam is 0.″3.

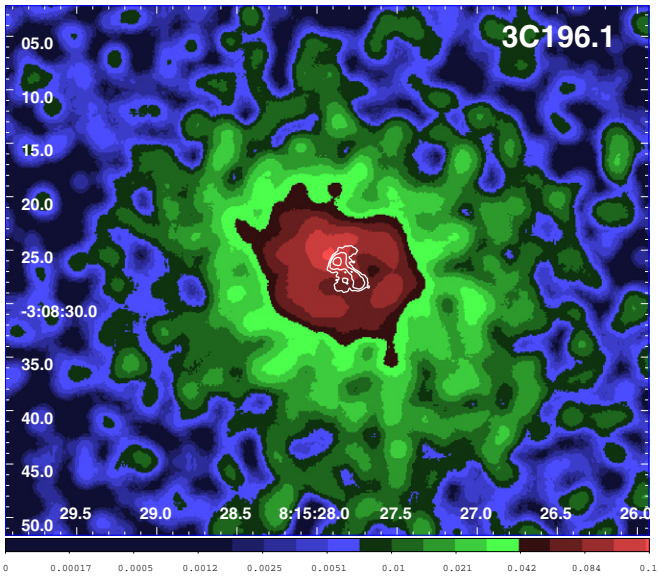

Figure 6. Low resolution X-ray image of 3C196.1 for the energy band 0.5–7 keV. The event file has been regridded to a pixel size of 0.″123 and smoothed with a Gaussian of FWHM = 2.″2. Brightness units are counts per pixel. The radio contours come from an 8.4 GHz VLA map kindly provided by C. C. Cheung and start at 0.5 mJy beam^{-1}, increasing by factors of four. The clean beam is 0.″3.

(Massaro et al. 2010) and with the distribution of the spectral index of the low redshift 3C radio sources (e.g., Hardcastle et al. 2009). In Figure 2, we show the $N_{\rm H}$ versus HR for the case of $\alpha_X = 0.5$ and 1.5 for the case of 3C 49.

Consequently, we calculated the $N_{\rm H}(z)$ estimates corresponding to the observed HR, including 1σ error, for the two values of α_X reported above in each source (see Figure 2 for additional details). Then, we considered the maximum and minimum values of these $N_{\rm H}(z)$ estimates to define the range where the "real" $N_{\rm H}(z)$ value could be corresponding to our estimate of the error on the intrinsic $N_{\rm H}(z)$. The ranges derived for each HR value are reported in Table 2 for the nuclei of AO12 sources.

We repeated the entire procedure for all the sources in our sample and for those presented in our previous work regarding the *Chandra* observations performed during Cycle 9 (Massaro et al. 2010). For the sake of consistency, we provide HR and $N_{\rm H}$ values in Table 3 for the nuclei of AO9 sources with less than 480 net counts (i.e., those unaffected by pile-up). We found that for the Cycle 9 sources, the results on the intrinsic absorption derived with our new hardness ratio method are in agreement with those previously presented.

Finally, we compared the results obtained from the X-ray spectral analysis with those derived from the HR study. We found good agreement between the two methods adopted in fact, all the values of the intrinsic absorption derived from the X-ray spectral analysis lie within the range of $N_{\rm H}(z)$ calculated via the HRs. The two cases of 3C 79 and 3C 234 were not compared

because given the low numbers of counts available their spectral parameters are poorly determined.

3.3. Source Details

3C 29 is a nearby FR I radio galaxy at redshift 0.0448, showing the typical optical elliptical morphology and having a compact nucleus in both the optical and ultraviolet. This source is probably an outlying member of the nearby cluster of galaxies A119, even if no significant companion appears within ∼100 kpc. The radio emission of 3C 29 is described in Feretti et al. (1999).

Although the available radio data are not adequate to trace the S jet back close to the nucleus, there is reasonably convincing evidence that the inner jet is detected in the X-ray band (see Figure 7). For a rectangular region extending to the SE (P.A. = 163°) from just outside the nucleus for 10″, we find 15 ± 4 net counts in the 0.5–2 keV energy range. For the 1–2 keV band, there are 9 counts in the "on" rectangle but none in the two adjoining background regions. For the strongest feature (s2.7), there are 8 counts (0.5–2 keV) within a circle of radius = 1″ and again, none in the two adjacent background circles.

3C 63 is an FR II radio galaxy that lies at redshift 0.175. Baum et al. (1988) report on faint emission regions transverse to the radio axis, particularly in the western region, together with the presence of an S-shaped filament in the optical images. Recently, Cheung (2007) has suggested that the radio morphology is that of an "X-shape" radio source. In the X-rays, we detect only the nucleus. There appears to be diffuse X-ray emission around the nucleus up to a radius ≈2.″5. There is also a slight X-ray excess coincident with the brightest part of the SW radio lobe.

3C 79 is an FR II radio galaxy associated with a luminous extended emission-line region (Fu & Stockton 2008), described as due to photoionization by the hidden active nucleus. It has also been classified as a high excitation galaxy (HEG; Buttiglione et al. 2009). There is no clear detection of extended emission.

3C 89 is a nearby WAT radio galaxy with an uncertain optical classification. It is hosted in a galaxy cluster that is clearly detected in the X-rays in our snapshot observations. An interesting aspect is that the brighter parts of the hot gas are between the arms of the radio source. In particular, there is a bright ridge of X-ray emission running back from the nucleus. The nuclear position is best defined by limiting the energy band to 5–7 keV. The X-ray source was detected by the *ROSAT* All-Sky Survey and identified as a cluster in Appenzeller et al. (1998). We did not report any measure of the X-ray flux for the core since it is contaminated by the radiation of the surrounding galaxy cluster. We note that the cluster of galaxies surrounding 3C 89 has the largest known X-ray cavity: ∼270 kpc in diameter (Sun et al. 2012). The X-ray images of 3C89 for the energy band 0.5–7 keV, with different resolution, are shown in Figures 3 and 4.

At a redshift of 0.1386, the scale is 2.386 kpc arcsec^{-1}. To include all of the X-ray emission, we chose to measure gross cluster parameters by defining a circle with a radius of 2′ (286 kpc). This circle is centered on the bright region at the center of the cluster and just touches the edge of the chip. We used the same size circle for the background, shifted 4′ to the SW. For our standard band of 0.5–7 keV, we find 1858 ± 58 net counts. We measured fluxmaps and find a total of 1.50×10^{-12} erg cm^{-2} s^{-1}, corresponding to a luminosity of 7.3×10^{43} erg s^{-1}. The uncertainties in these values are of the order of 7%.

Using the same regions, we performed a standard spectral analysis using Sherpa with the absorption frozen at the galactic value. Since we noted that the flux distribution was weighted toward the higher energies (more than half of the total flux is above 2 keV), we tried fits for both an absorbed power law and an absorbed APEC model. Both fits gave reduced χ^2 values less than 1. The spectral index for the power-law fit is 0.62 ± 0.08 and the APEC model (for a frozen solar abundance of unity) gives $kt = 5.7 \pm 1.6$ keV. Approximately one-fifth of the total luminosity comes from the bright central region between the radio tails.

3C 93.1 is a CSS radio source that shows an extended optical narrow-line emitting region surrounding the core for about 3.8 kpc, primarily toward the northeast side (Tremblay et al. 2009). We clearly detected the X-ray core but we did not find any evidence of extended structures.

3C 130 is a classical FR I radio galaxy at redshift 0.1090. The optical morphology is clearly elliptical without any peculiarity. The core is detected in the X-rays and it also shows significant extended X-ray emission around its central region.

3C 166 is an FR II radio galaxy optically classified as a low excitation galaxy (LEG; Buttiglione et al. 2009). It shows an unusual radio structure featuring two lobes with very different morphologies (Spangler & Bridle 1982). The source has a bright unresolved infrared nucleus (Floyd et al. 2008). We did not detect any extended emission in the X-ray.

3C 180 is a classical FR II radio source optically classified as HEG (Buttiglione et al. 2009). It is hosted in a giant elliptical galaxy (Madrid et al. 2006) and according to McCarthy et al. (1995) it is also a member of a cluster of galaxies. We do not detect any clear signatures of X-ray emission arising from the surrounding galaxy cluster.

3C 196.1 lies within a cluster of galaxies cataloged in the *ROSAT* bright source catalog and by Kocevski et al. (2007) in their search for clusters in the zone of avoidance. With an exposure of 8 ks, there are 3700 net counts detected in a circle of radius 90″. The global temperature estimate for the entire cluster is 4.2 ± 0.2 keV. Restricting the spectral analysis to smaller circles, the temperature drops: 3.4 ± 0.2 for $r = 20''$, 3.0 ± 0.3 for $r = 7''$, and 1.0 keV for $r = 1.''5$, the last value centered on the brightest part of the inner structure. With a redshift of 0.198, the luminosity distance is 936 Mpc and the angular scale is 3.16 kpc arcsec^{-1}. The luminosity in the band 0.5–7 keV is 3×10^{44} erg s^{-1}. Some further aspects of this cluster have been discussed by Harris et al. (2011).

The radio source has been classified as an FR II and is associated with the dominant galaxy of the cluster. The radio power and optical magnitude of 3C 196.1 place it well above the dividing line between FR I and FR II of Owen & Laing (1989). However, its morphology is strikingly different from the prototype FR II, Cygnus A, which also resides in a cluster. Unlike Cygnus A with a total size of 120 kpc (from hot spot to hot spot), the extent of 3C196.1 is only 12 kpc. Thus, it probably is wholly within the cD galaxy, although we cannot be sure of this since the irregular morphology precludes even a reasonable guess at projection effects. The physical size of 3C196.1 could be much larger than its projected size. The best description of this source with the available 0.″3 resolution is an "HYMORS," a so-called HYbrid Morphology Radio Source (Gopal-Krishna & Wiita 2000; Kharb et al. 2010). In the case of 3C196.1, the SW side is jet-like (i.e., FR I) whereas the NE side appears to be a classical FR II lobe with a brightness enhancement toward the edge. Perhaps, however, this feature

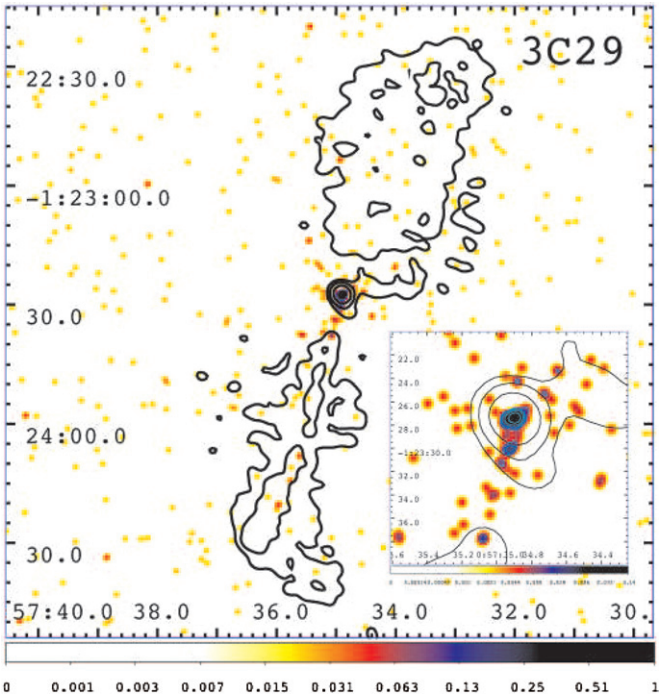

Figure 7. X-ray image of 3C 29 for the energy band 0.5–7 keV. The event file has been regridded to a pixel size of 0.″246 and smoothed with a Gaussian of FWHM = 1.″4. For the inset, the pixel size is 0.0615 and the FWHM of the smoothing function is 0.″8. X-ray contours (white or cyan) start at 0.01 counts pixel^{-1} and increase by factors of two. The radio contours (black) come from an 8.4 GHz VLA map downloaded from the NVAS and start at 0.9 mJy beam^{-1}, increasing by factors of four. The clean beam is 3.″0 × 2.″7 with major axis in P.A. = 43°.

(A color version of this figure is available in the online journal.)

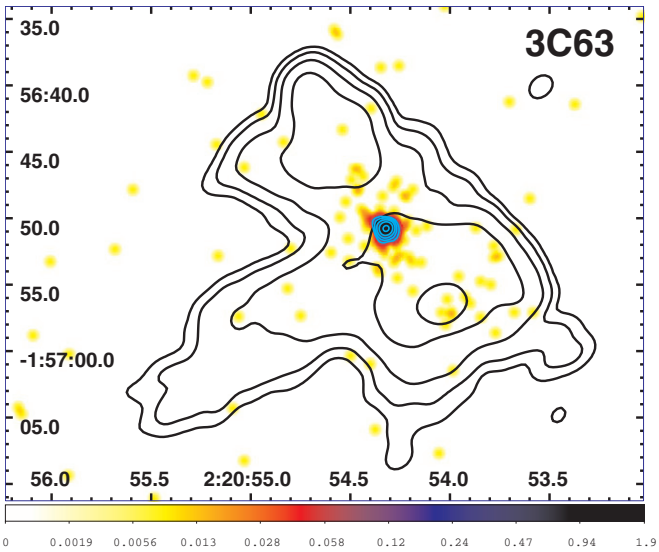

Figure 8. X-ray image of 3C63 for the energy band 0.5–7 keV. The event file has been regridded to a pixel size of 0.″0615 and smoothed with a Gaussian of FWHM = 0.″65. X-ray contours (white or cyan) start at 0.1 counts pixel^{-1} and increase by factors of two. The radio contours (black) come from a 1.4 GHz map downloaded from the NVAS and start at 0.4 mJy beam^{-1}, increasing by factors of four. The clean beam is 1.″9 × 1.″4.

(A color version of this figure is available in the online journal.)

is not a true hot spot, but rather the location where the NE jet impacts the higher density intracluster medium, as indicated by the peak X-ray brightness. In Figures 5 and 6, there appears to be a "ghost cavity" wrapping around the SW jet/lobe.

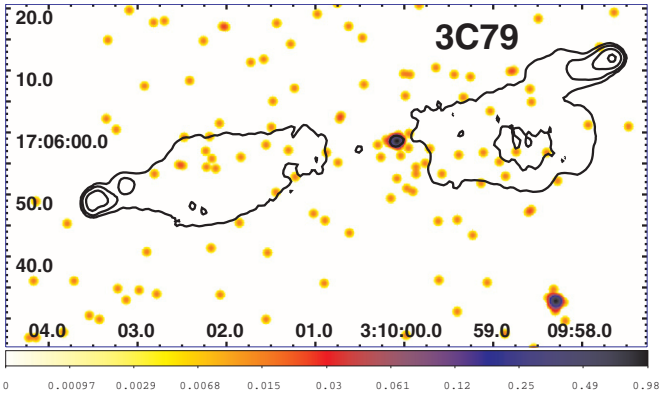

Figure 9. X-ray image of 3C79 for the energy band 0.5–7 keV. The event file has been regridded to a pixel size of 0.″123 and smoothed with a Gaussian of FWHM = 1.″0. The radio contours (black) come from a 1.4 GHz map downloaded from the DRAGN Web site and start at 4 mJy beam^{-1}, increasing by factors of four. The clean beam is 1.″5.

(A color version of this figure is available in the online journal.)

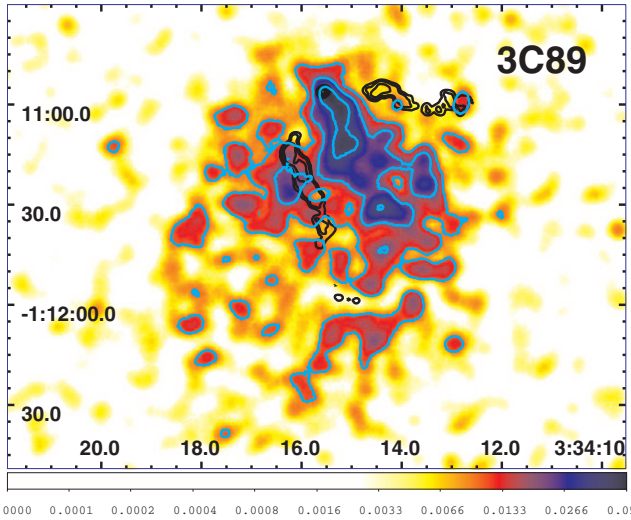

Figure 10. X-ray image of 3C89 for the energy band 0.5–7 keV. The event file has been regridded to a pixel size of 0.″246 and smoothed with a Gaussian of FWHM = 5.″5. X-ray contours (white or cyan) start at 0.01 counts pixel^{-1} and increase by factors of two. The radio contours (black) come from a 1.5 GHz map downloaded from the NVAS and start at 0.5 mJy beam^{-1}, increasing by factors of four. The clean beam is 1.″5 × 1.″3 FWHM with major axis at P.A. = −57°.

(A color version of this figure is available in the online journal.)

The steep (radio) spectrum "S lobe" impinges on part of this cavity.

Since the Galactic latitude of 3C196.1 is 17°, the optical attributes of the cluster are not well determined. The host galaxy is a cD, the dominant galaxy of a group of 14 others that lie within about 350 kpc from its core (Baum et al. 1988). Madrid et al. (2006) show that its near-infrared image is elliptical, presenting an elongated structure northeast to southwest, which is the same direction as the radio emission. The same morphology is seen in the optical (de Koff et al. 1996; Baum et al. 1988). [O III] emission lines are observed in two localized regions cospatial with the elongated bright core (Tremblay et al. 2009).

3C 198 is classified as FR II on the basis of its radio luminosity at 178 MHz, as reported in Spinrad et al. (1985). With the currently available radio data, we have been unable to locate a

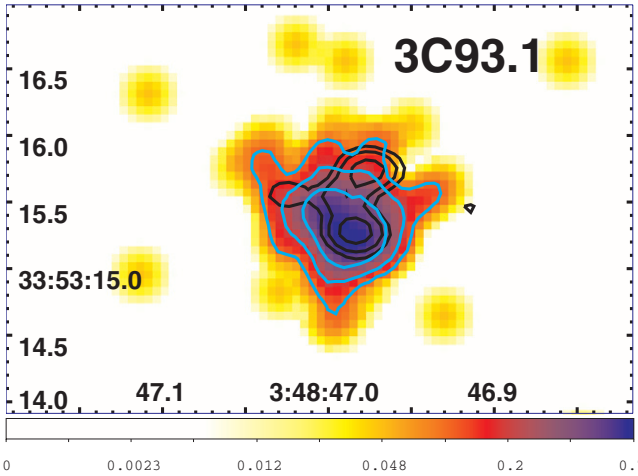

Figure 11. X-ray image of 3C93.1 for the energy band 0.5–7 keV. The event file has been regridded to a pixel size of 0.″0615 and smoothed with a Gaussian of FWHM = 0.″3. X-ray contours (white or cyan) start at 0.1 counts pixel^{-1} and increase by factors of two. The radio contours (black) come from an 8.4 GHz VLA map downloaded from the NVAS and start at 10 mJy beam^{-1}, increasing by factors of two. The clean beam is 0.″3 × 0.″2 with major axis at P.A. = 90°.

(A color version of this figure is available in the online journal.)

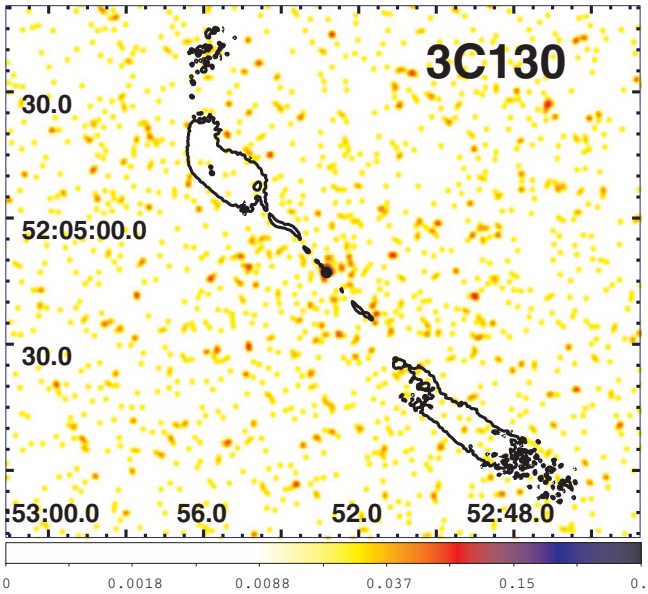

Figure 12. X-ray image of 3C130 for the energy band 0.5–7 keV. The event file has been regridded to a pixel size of 0.″246 and smoothed with a Gaussian of FWHM = 1.″4. The radio contours (black) come from an 8.4 GHz VLA map kindly supplied by M. Hardcastle and start at 0.1 mJy beam^{-1}, increasing by factors of four. The clean beam is 0.″6.

(A color version of this figure is available in the online journal.)

radio nucleus. The data in Table 2 come from measuring a weak X-ray source at the NED position of the optical galaxy.

3C 223 is a classical FR II–HEG radio galaxy whereas the near-infrared image shows an asymmetric galaxy, slightly elongated from the northeast to southwest side (Madrid et al. 2006). We detected only the X-ray core in our *Chandra* snapshot survey.

3C 234 is an FR II radio galaxy optically classified as HEG. Its optical images (Tremblay et al. 2009) show an elongated

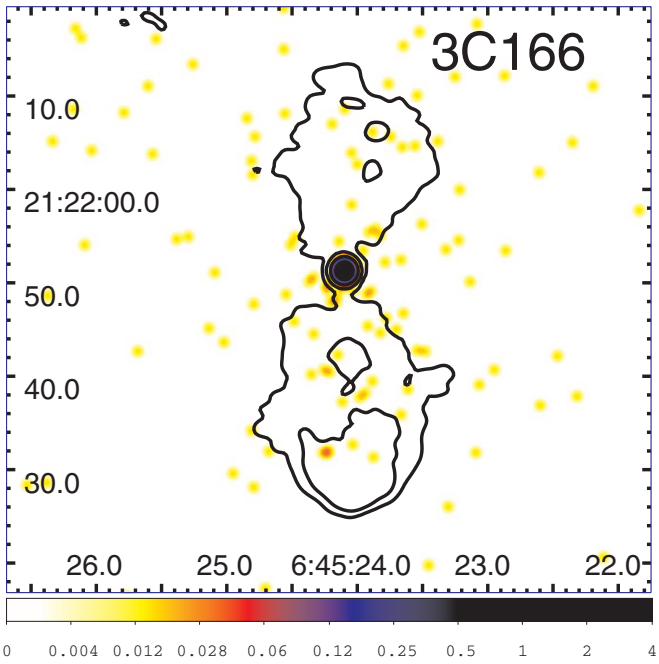

Figure 13. X-ray image of 3C166 for the energy band 0.5–7 keV. The event file has been regridded to a pixel size of 0.″123 and smoothed with a Gaussian of FWHM = 1.″0. The radio contours (black) come from a 1.4 GHz map downloaded from NED and start at 2 mJy beam^{-1}, increasing by factors of four. The clean beam is 1.″3.

(A color version of this figure is available in the online journal.)

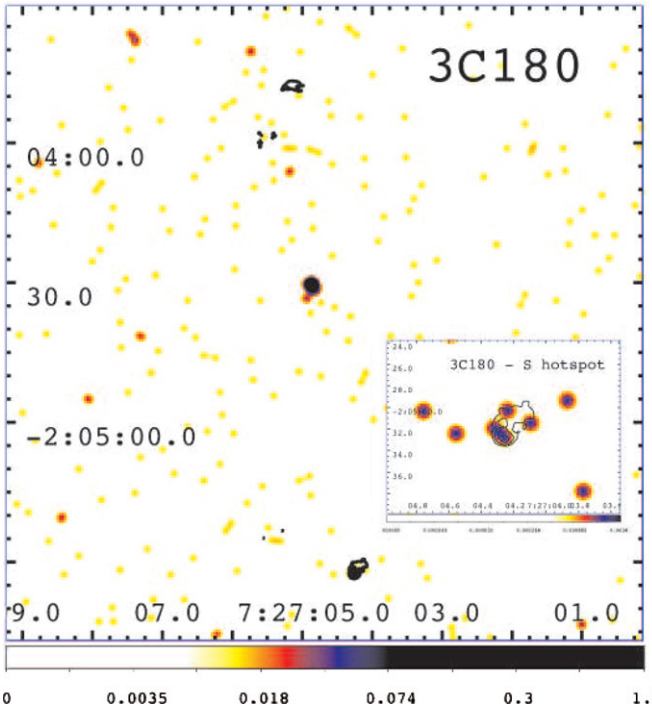

Figure 14. X-ray image of 3C180 for the energy band 0.5–7 keV. The event file has been regridded to a pixel size of 0.″246 and smoothed with a Gaussian of FWHM = 2″. The radio contours (black) come from an 8.4 GHz VLA map kindly supplied by C. C. Cheung and start at 0.5 mJy beam^{-1}, increasing by factors of four. The clean beam is 0.″36. For the inset of the S hot spot, the pixel size is 0.″06 and the smoothing function has an FWHM = 1.″4.

(A color version of this figure is available in the online journal.)

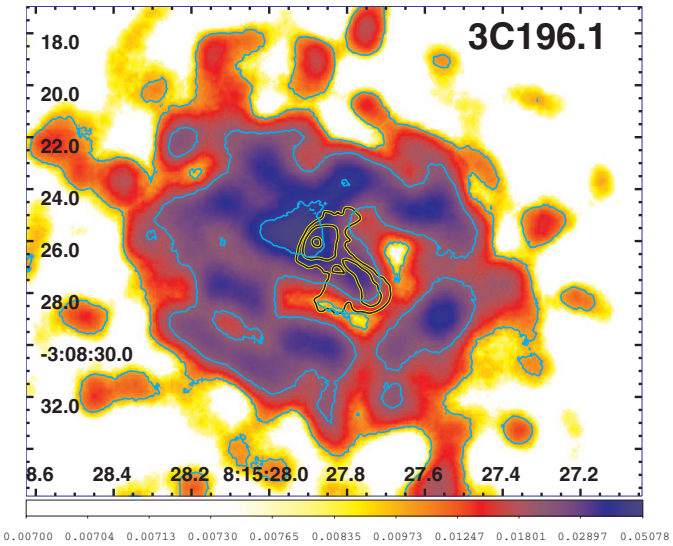

Figure 15. X-ray image of 3C196.1 for the energy band 0.5–7 keV. The pixel size is 0.″492 and the map has been smoothed with a Gaussian of FWHM = 11″. X-ray contours (white or cyan) start at 0.01 counts pixel^{-1} and increase by factors of two. The radio contours (black, outlined in yellow) come from an 8.4 GHz VLA map kindly supplied by C. C. Cheung and the contours start at 0.75 mJy beam^{-1}, increasing by factors of four. The clean beam is 0.″3.

(A color version of this figure is available in the online journal.)

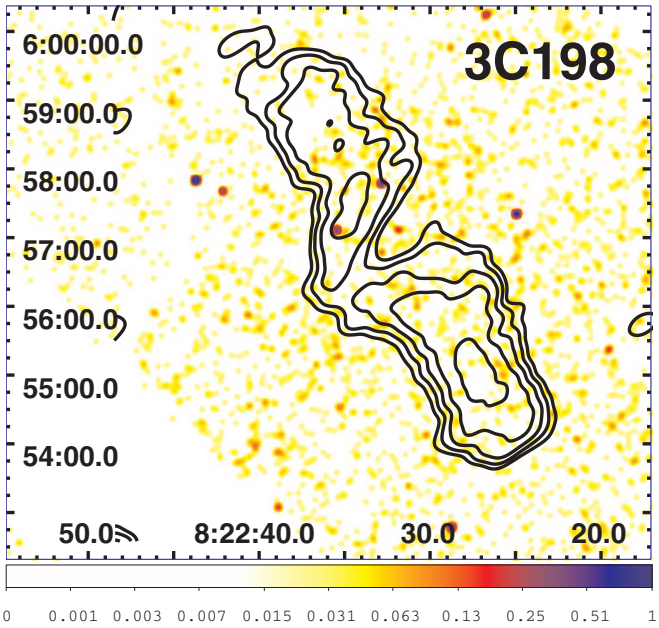

Figure 16. X-ray image of 3C198 for the energy band 0.5–7 keV. The event file has been blocked by a factor of two so the pixel size is 0.″984. The map has been smoothed with a Gaussian of FWHM = 11.″8. The radio contours (black) come from a 4.9 GHz map produced from the NRAO archives and start at 0.5 mJy beam^{-1}, increasing by factors of two. The clean beam is 25″ × 14″ with major axis in P.A. = −52°. Since no nuclear emission could be isolated in the radio, the X-ray map has not been registered. A gap between ACIS chips runs through the N lobe and the edge of the S3 chip is obvious to the SE of the source.

(A color version of this figure is available in the online journal.)

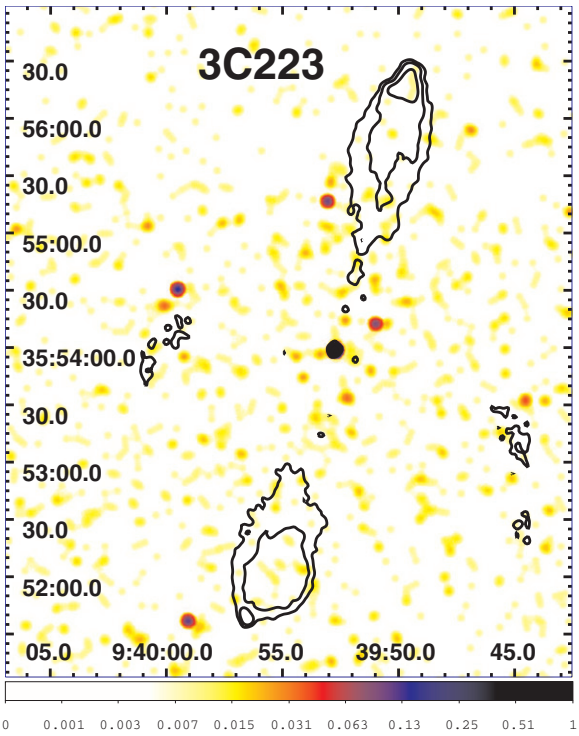

Figure 17. X-ray image of 3C 223 for the energy band 0.5–7 keV. The smoothing function applied is a Gaussian of FWHM = 5.″2. The radio contours (black) come from an 8.4 GHz VLA map kindly supplied by M. Hardcastle and start at 0.2 mJy beam^{-1}, increasing by factors of four. The clean beam is 2.″5. The N radio hot spot falls on chip S2.

(A color version of this figure is available in the online journal.)

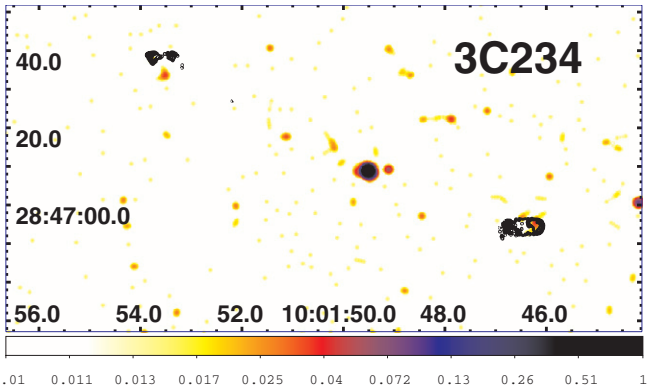

Figure 18. X-ray image of 3C 234 for the energy band 0.5–7 keV. The event file has been regridded to a pixel size of 0.″243 and smoothed with a Gaussian of FWHM = 2.″0. The radio contours (black) come from an 8.4 GHz VLA map kindly supplied by C. C. Cheung and start at 0.4 mJy beam^{-1}, increasing by factors of four. The clean beam is 0.″4.

(A color version of this figure is available in the online journal.)

emission line region that includes a tidal arm (Carleton et al. 1984) that appears to be roughly parallel with that of the radio jet axis on large scales (see also Privon et al. 2008 for more details). The SW hot spot is clearly detected in the X-ray band. The X-ray spectral analysis of the nuclear emission in 3C 234 has been presented by Piconcelli et al. (2008). They found a thermal-dominated X-ray spectrum, rich in emission lines, confirming the presence of a hidden quasar in this source and claiming that the origin of the X-ray emission in radio-loud AGNs with high-excitation optical lines does not always arise from jet non-thermal radiation.

3C 258 is a well-known CSS radio galaxy with an uncertain redshift estimate (Floyd et al. 2008).

3C 284 is a classical FR II–HEG radio source, hosted by a disturbed elliptical galaxy at redshift 0.2394 with a southeast tidal

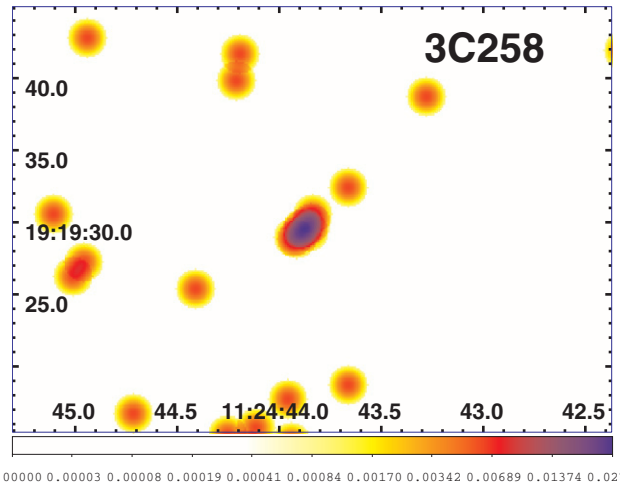

Figure 19. X-ray image of 3C 258 for the energy band 0.5–7 keV. The event file has been regridded to a pixel size of 0.″123 and smoothed with a Gaussian of FWHM = 1.″6. There are no radio contours shown because the total radio intensity consists of a close (unequal) double with separation of 0.″1. See the 5 GHz MERLIN contours on NED. Our detection of the nucleus of the galaxy comprises only 7 counts and is the source at the center of the figure.

(A color version of this figure is available in the online journal.)

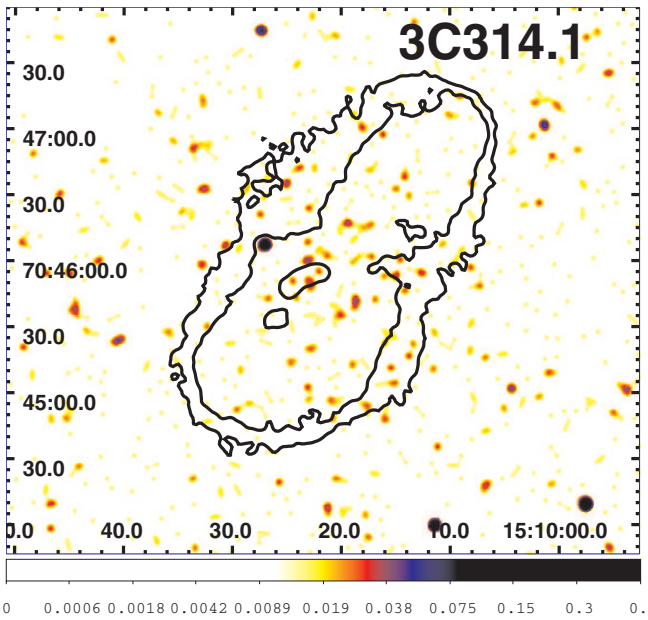

Figure 21. X-ray image of 3C 314.1 for the energy band 0.5–7 keV. The pixel size is 0.″492 and the map has been smoothed with a Gaussian of FWHM = 4.″0. The radio contours (black) come from a 1.5 GHz map downloaded from the DRAGN Web site and start at 0.3 mJy beam^{-1}, increasing by factors of four. The clean beam is 4.″2. We used the point source which lies near the E edge of the radio structure to register the X-ray image so as to match the radio map.

(A color version of this figure is available in the online journal.)

tail toward its most prominent companion (Floyd et al. 2008). Only the X-ray core is detected in our *Chandra* observation.

3C 314.1 is an FR I–LEG radio galaxy hosted in an elliptical galaxy that shows an infrared elongated structure from the east–northeast side to the west–southwest (Madrid et al. 2006).

3C 319 is an FR II radio galaxy, the only source in our current sample for which we did not detect X-ray emission from the nucleus. The NE hot spot is detected with four counts. The galaxy is also very faint in the *HST* optical images with an extended emission line region dominated by the [O III] line, which is more compact than the Hα+[N II] one (Tremblay et al. 2009).

3C 357 is an FR II–LEG radio galaxy at redshift 0.1662 with a projected angular size corresponding to ∼250 kpc (Fanti et al. 1997; Harvanek & Hardcastle 1998). It shows an optical emission line region of a few arcseconds in scale, extending from the nucleus along the radio axis (McCarthy et al. 1995). Both de Koff et al. (1996) and Capetti et al. (2000) reported on filamentary dust lanes in the southwestern region. The host galaxy is a classical giant elliptical with no remarkable features (Floyd et al. 2008). In our *Chandra* snapshot observation, we clearly detected the core emission but no extended radiation around the core or associated with the hot spots has been observed.

3C 379.1 is an FR II–HEG radio galaxy hosted in an elongated elliptical galaxy as seen in the near-IR *HST* images (Floyd et al. 2008).

3C 402 has two bright galaxies separated by ≈2′ in declination and each appears to be a radio galaxy. We suspect that the large-scale radio structures are superposed. Both nuclei are detected in radio and X-rays and both are somewhat extended. With the radio maps available to us, our registration of the X-ray map is less secure than usual. This is because of the difficulty of

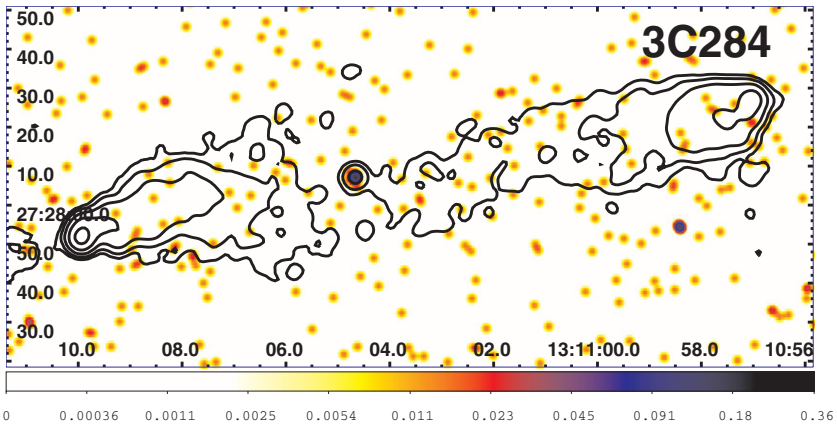

Figure 20. X-ray image of 3C 284 for the energy band 0.5–7 keV. The event file has been regridded to a pixel size of 0.″246 and smoothed with a Gaussian of FWHM = 2.″0. The radio contours (black) come from an 8.0 GHz map kindly supplied by M. Hardcastle and start at 0.1 mJy beam^{-1}, increasing by factors of four. The clean beam is 3.″6.

(A color version of this figure is available in the online journal.)

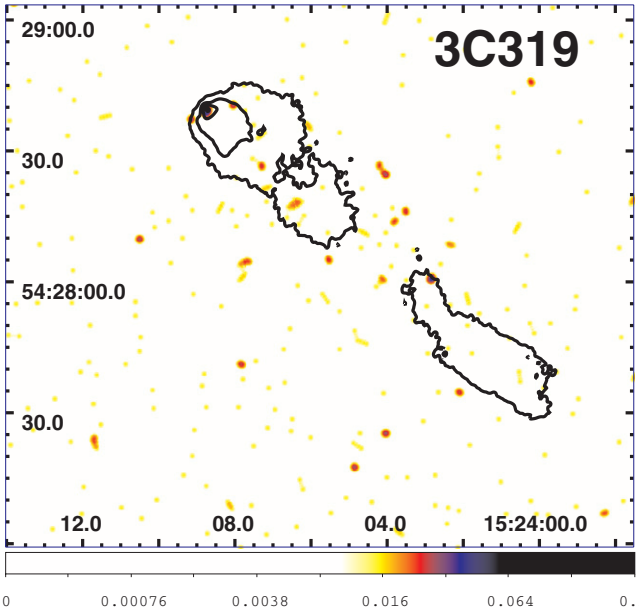

Figure 22. X-ray image of 3C 319 for the energy band 0.5–7 keV. The event file has been regridded to a pixel size of 0.″246 and smoothed with a Gaussian of FWHM = 2.″0. The radio contours (black) come from an 8.4 GHz VLA map kindly provided by M. Hardcastle and start at 0.1 mJy beam^{-1}, increasing by factors of four. The clean beam is 0.″9. Since the nucleus has not been detected in either X-rays or radio, the map is not registered. We "detect" the N radio hot spot with 4 counts.

(A color version of this figure is available in the online journal.)

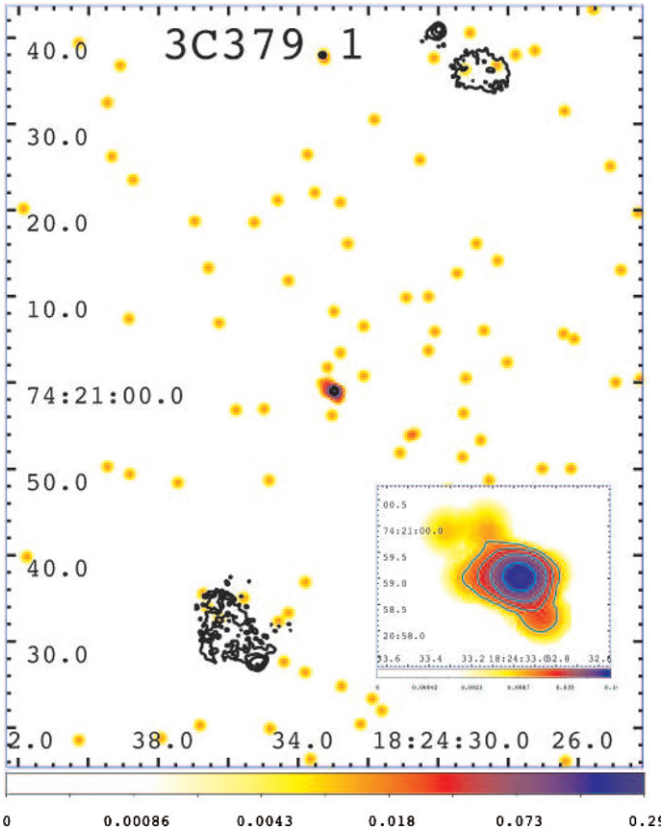

Figure 24. X-ray image of 3C 379.1 for the energy band 0.5–7 keV. The event file has been regridded to a pixel size of 0.″123 and smoothed with a Gaussian of FWHM = 1.″0. The radio contours (black) come from an 8.4 GHz VLA kindly provided by C. C. Cheung and start at 0.2 mJy beam^{-1}, increasing by factors of four. The clean beam is 0.″35. The 30 counts comprising the nucleus are shown in the inset. The pixel size is 0.″0615 and the smoothing function has an FWHM of 0.″65. X-ray contours begin at 0.012 counts pixel^{-1} and increase by factors of two.

(A color version of this figure is available in the online journal.)

determining the location of the peak brightness for an extended feature and because the radio maps have a large beam size. The X-ray nucleus of 402N has a 2″ long extension to the SW, which could be a jet.

3C 403.1 is a double FR II radio source with an LEG optical classification (Buttiglione et al. 2009).

3C 410 is an FR II broad-line radio galaxy (Buttiglione et al. 2009) with a redshift of 0.2485. The X-ray nucleus has to be shifted by 1″ in declination in order to align the central component of the radio triple with the X-ray. In our experience in registering well over a hundred *Chandra* observations, the usual shift required to align radio and X-ray nuclei is between 0.″2 and 0.″3, and almost never larger than 0.″4 (see also Section 2). However, since the absolute pointing determined by the *Chandra* star trackers is occasionally off by ≈1″ (T. Aldcroft 2011, private communication), we believe the registration performed is correct.

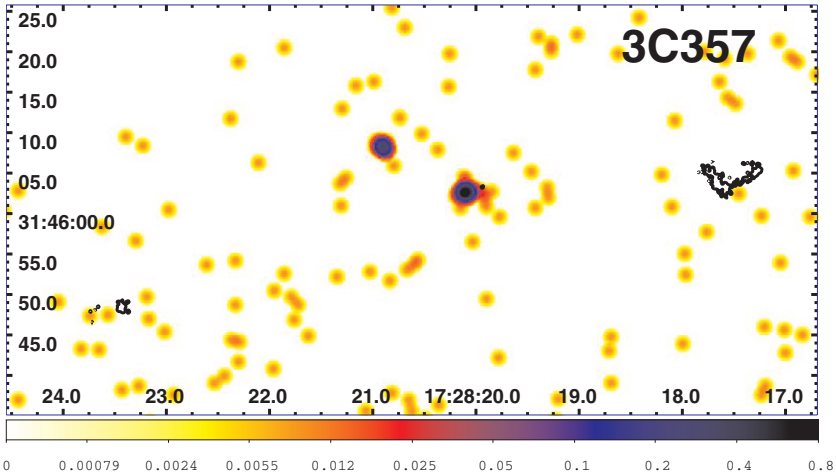

Figure 23. X-ray image of 3C 357 for the energy band 0.5–7 keV. The event file has been regridded to a pixel size of 0.″123 and smoothed with a Gaussian of FWHM = 1.″3. The radio contours (black) come from an 8.4 GHz VLA map kindly supplied by C. C. Cheung and start at 0.4 mJy beam^{-1}, increasing by factors of four. The clean beam is 0.″33. The nucleus is the SW of the pair of bright sources near the field center.

(A color version of this figure is available in the online journal.)

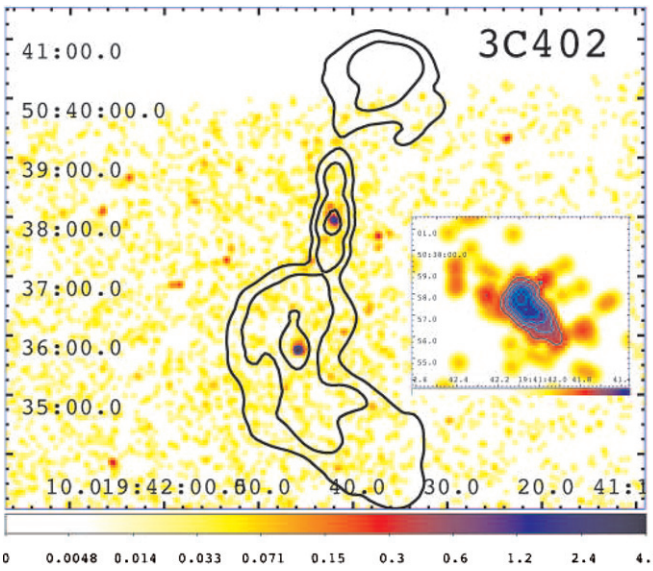

Figure 25. X-ray image of 3C 402 for the energy band 0.5–7 keV. The event file has been regridded to a pixel size of 0.″984 and smoothed with a Gaussian of FWHM = 5.″8. The radio contours (black) come from a 1.5 GHz map downloaded from the NVAS and start at 4 mJy beam^{-1}, increasing by factors of four. The clean beam is 19.″7 × 13″ with major axis in P.A. = 90°. There are two bright galaxies, each of which is detected in X-rays, and both appear to contribute to the complex radio morphology. The N radio lobe extends off the ACIS S3 chip. Since neither nucleus (both in radio and X-rays) is point-like, the registration of the X-ray image is not as accurate as usual. An X-ray image of the N nucleus is shown in the inset. The pixel size is 0.″0615 and the smoothing function has FWHM = 0.″8. Contours are linear: 0.015, 0.025, . . . , 0.055 counts pixel^{-1}. The structure defined by the contours contains about 50 counts.

(A color version of this figure is available in the online journal.)

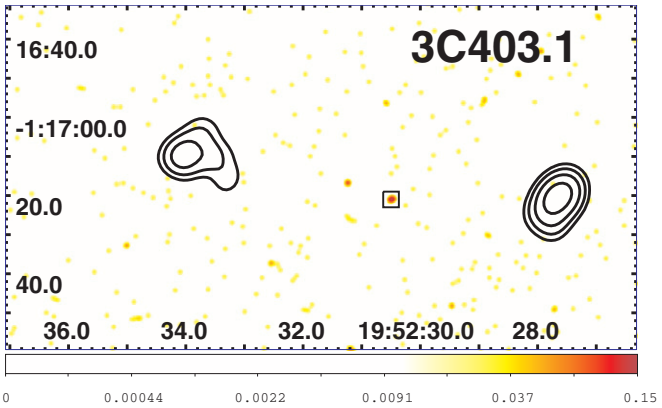

Figure 26. X-ray image of 3C 403.1 for the energy band 0.5–7 keV. The event file has been regridded to a pixel size of 0.″246 and smoothed with a Gaussian of FWHM = 1.″4. The radio contours (black) come from a 0.3 GHz map and start at 16 mJy beam^{-1}, increasing by factors of two. The clean beam is 7.″0 × 6.″2 with major axis in P.A. = −20°. The small box indicates the NED position and we find a weak source there.

(A color version of this figure is available in the online journal.)

3C 424 is a nearby FR I–LEG that lies at redshift 0.127 in a dense environment, with numerous companions clearly detected in the optical *HST* image (de Koff et al. 1996). The radio source apparently is close to the edge of a galaxy cluster (de Koff et al. 1996), however, cluster emission is not detected in the X-ray band. The X-ray nucleus has an extension 0.″6 to the NW which might be the inner segment of a jet.

3C 430 is an FR II–LEG radio galaxy hosted in an elongated elliptical galaxy at redshift 0.0541, with a dust lane around the

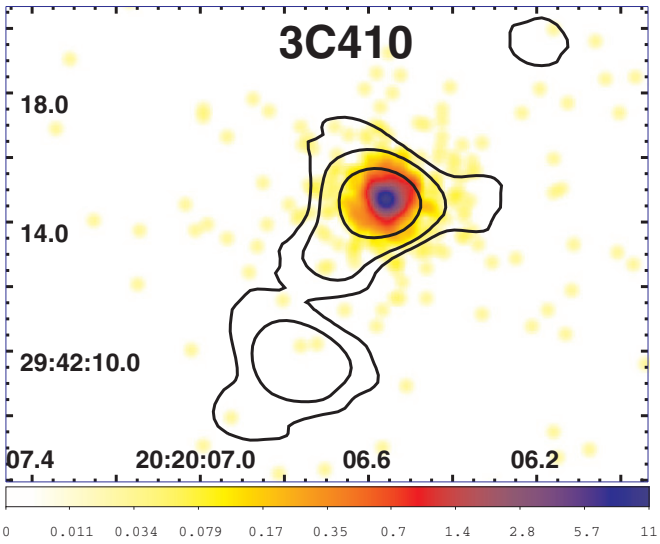

Figure 27. X-ray image of 3C 410 for the energy band 0.5–7 keV. The event file has been regridded to a pixel size of 0.″0615 and smoothed with a Gaussian of FWHM = 0.″36. The radio contours (black) come from a 43 GHz map downloaded from the NVAS and start at 6 mJy beam^{-1}, increasing by factors of four. The clean beam is 1.″7. The shift in the X-ray map required to align the X-ray source with the central component of a 5 GHz map is 1″ in declination, far larger than normal.

(A color version of this figure is available in the online journal.)

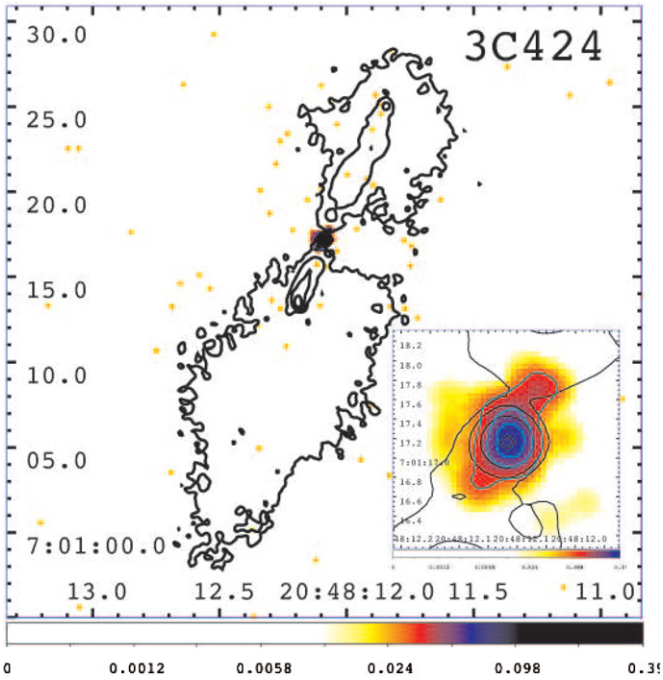

Figure 28. X-ray image of 3C 424 for the energy band 0.5–7 keV. The event file has been regridded to a pixel size of 0.″0615 and smoothed with a Gaussian of FWHM = 0.″36. The radio contours (black) come from an 8.5 GHz map kindly provided by M. Hardcastle and start at 0.05 mJy beam^{-1}, increasing by factors of four. The clean beam is 0.″25. The inset shows a blowup of the nucleus. Contours are linear: 0.1, 0.2, 0.3, and 0.4 counts pixel^{-1}. The smoothing function is a Gaussian of FWHM = 0.″36.

(A color version of this figure is available in the online journal.)

nucleus that could be responsible for absorption in the X-ray band as suggested by the lack of X-ray counts in the soft band.

3C 436 is a typical FR II–HEG hosted in an elliptical galaxy elongated in the same direction as its radio structure (Madrid et al. 2006). For the nucleus, 25 of the 41 total counts lie between

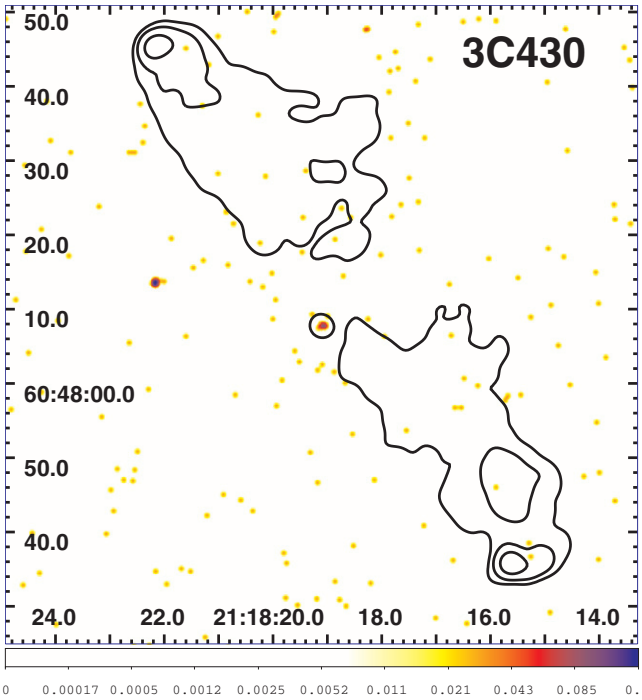

Figure 29. X-ray image of 3C 430 for the energy band 0.5–7 keV. The event file has been regridded to a pixel size of 0.″123 and smoothed with a Gaussian of FWHM = 0.″7. The radio contours (black) come from a 4.9 GHz map downloaded from the NVAS and start at 1 mJy beam^{-1}, increasing by factors of four. The clean beam is 1.″3.

(A color version of this figure is available in the online journal.)

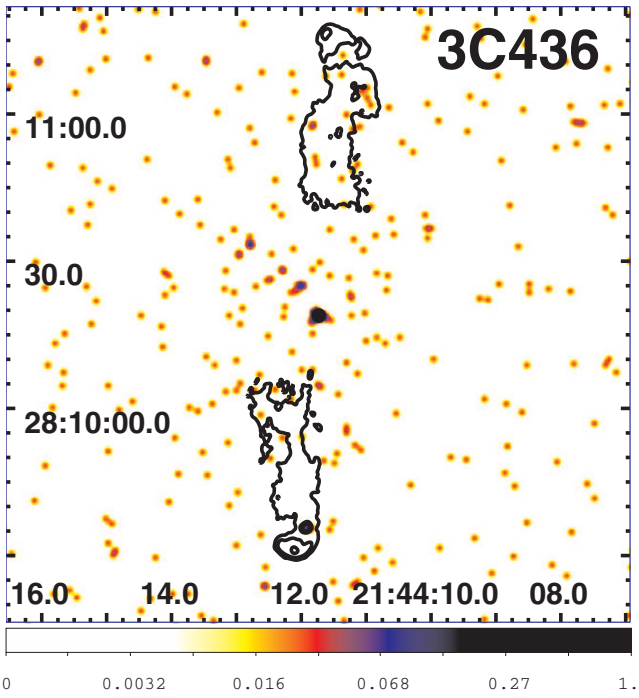

Figure 30. X-ray image of 3C 436 for the energy band 0.5–7 keV. The event file has been regridded to a pixel size of 0.″246 and smoothed with a Gaussian of FWHM = 1.″4. The radio contours (black) come from an 8.4 GHz VLA map kindly supplied by M. Hardcastle and start at 0.2 mJy beam^{-1}, increasing by factors of four. The clean beam is 0.″75. The hot spot near the tip of the S lobe is detected with four counts.

(A color version of this figure is available in the online journal.)

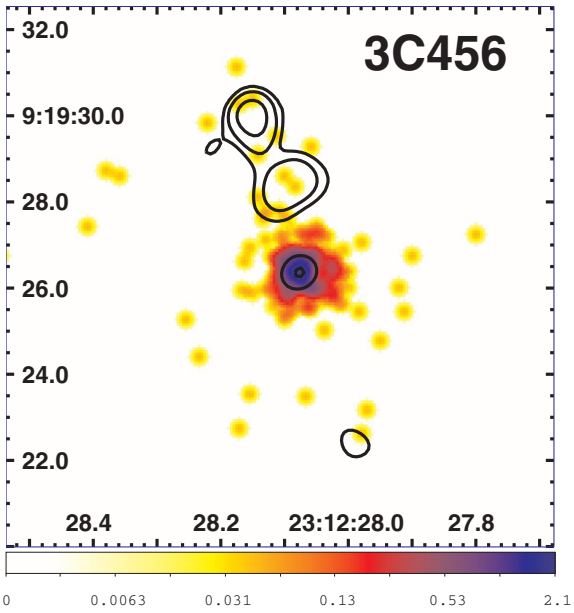

Figure 31. X-ray image of 3C 456 for the energy band 0.5–7 keV. The event file has been regridded to a pixel size of 0.″0615 and smoothed with a Gaussian of FWHM = 0.″3. The radio contours (black) come from a 4.9 GHz map kindly supplied by M. Hardcastle and start at 5 mJy beam^{-1}, increasing by factors of four. The clean beam is 0.″5.

(A color version of this figure is available in the online journal.)

4 and 6 keV. We detect what might be described as the "primary" radio hot spot close to the tip of the S lobe.

3C 456 is an FR II–HEG radio galaxy at redshift 0.233. In the X-rays, we detected only the nucleus which appears to be highly absorbed (see also Section 2.2 for additional details).

3C 458 is an FR II–HEG radio galaxy. We detect the NE hot spot with four counts.

3C 459 is an FR II broad-line radio galaxy. The host galaxy is dominated by a young stellar population (Tadhunter et al. 2002) and its IR structure has been suggested to be the result of a recent merger (Floyd et al. 2008). The radio source is small and very asymmetric (Morganti et al. 1999). The high resolution radio map (Morganti et al. 1993) reveals a weak western component (see Figure 33). The extended X-ray emission around the nucleus is mostly on the E side, coincident with the E radio lobe.

4. SUMMARY

We have presented our X-ray analyses of the second half of the 3C low redshift sample (i.e., $z < 0.3$) observed by *Chandra* during Cycle 12. Since we waived proprietary rights, X-ray data for all extragalactic 3C sources with $z < 0.3$ are now available to the community for statistical analyses based on a complete, unbiased sample. In addition, we have found several sources worthy of more detailed study, such as 3C 89, for which follow-up *Chandra* observations totaling 68 ks with ACIS-I have already been performed in Cycle 13 (Sun et al. 2012).

We have constructed fluxmaps for all the X-ray observations and given photometric results for the nuclei and other radio structures (i.e., jet knots, hot spots, lobes). For the stronger nuclei, we have employed the usual X-ray spectral analysis and compared the column densities of intrinsic absorption to those obtained from the hardness ratio analysis (see Section 3.2). As expected, X-ray emission was detected for all the nuclei except for 3C 319, a small FR II radio galaxy. A sizable fraction ($\sim$1/3) of our 3C sources shows evidence for significant intrinsic absorption (see Sections 2.2 and 3.2 for more details).

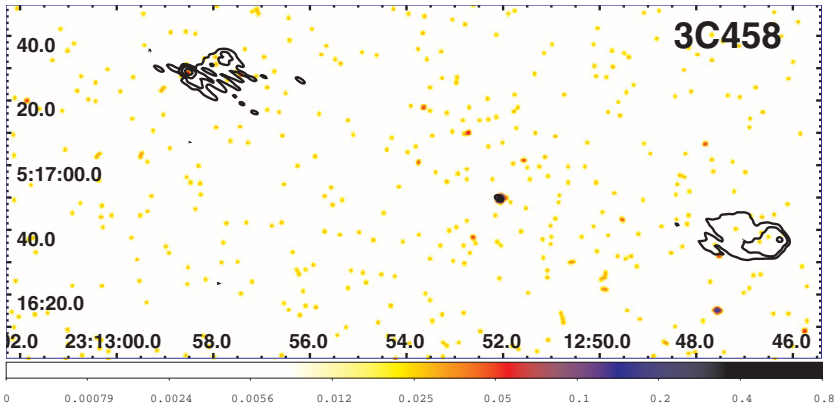

Figure 32. X-ray image of 3C 458 for the energy band 0.5–7 keV. The event file has been regridded to a pixel size of 0.″246 and smoothed with a Gaussian of FWHM = 1.″5. The radio contours (black) come from a 4.9 GHz map downloaded from the NVAS and start at 1 mJy beam^{-1}, increasing by factors of four. The clean beam is 2.″3 × 1.″4 with major axis in P.A. = 65°. We detect the NE hot spot with four counts.

(A color version of this figure is available in the online journal.)

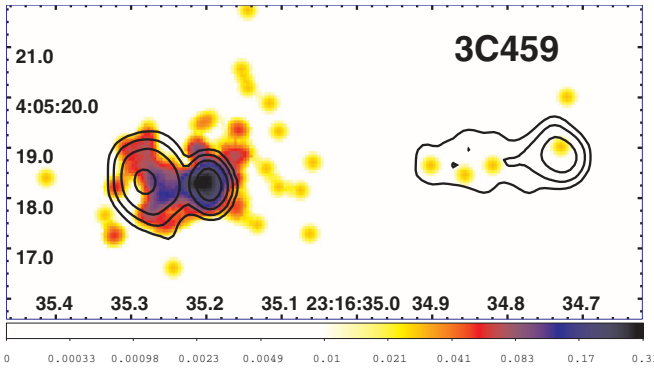

Figure 33. X-ray image of 3C 459 for the energy band 0.5–7 keV. The event file has been regridded to a pixel size of 0.″0615 and smoothed with a Gaussian of FWHM = 0.″36. The radio contours (black) come from a 4.9 GHz map downloaded from the NVAS and start at 2 mJy beam^{-1}, increasing by factors of four. The clean beam is 0.″5 × 0.″4 with major axis in P.A. = 9°.

(A color version of this figure is available in the online journal.)

Among our 3C *Chandra* observations, we detected two CSS radio sources: 3C 93.1 and 3C 258, one WAT radio galaxy, 3C 89, hosted in the cluster of galaxies with the largest known X-ray cavity (Sun et al. 2012) and the X-ray emission of the galaxy cluster surrounding 3C 196.1. We also detected X-ray emission from three radio hot spots and, in the case of 3C 459, emission coincident with the eastern radio lobe (see Section 3). Finally, we found X-ray emission cospatial with two radio jets: 3C 29 and 3C 402.

We thank the anonymous referee for useful comments that led to improvements in the paper. We wish to honor the memory of our great friend and colleague David Axon, who has been the steadfast inspiration and participant in this and many other key papers that through many years of dedicated efforts have led to significant breakthroughs and greater understanding of the physics of active galaxies. He will be greatly missed by all of us. We are grateful to M. Hardcastle and C. C. Cheung for providing several radio maps of the 3C sources. We also thank C. C. Cheung and S. Bianchi for helpful discussions. This research has made use of NASA's Astrophysics Data System; SAOImage DS9, developed by the Smithsonian Astrophysical Observatory, and the NASA/IPAC Extragalactic Database (NED), which is operated by the Jet Propulsion Laboratory, California Institute of Technology, under contract with the National Aeronautics and Space Administration. Several radio maps were downloaded from the NVAS (NRAO VLA Archive Survey) and from the DRAGN Web site.[20] The National Radio Astronomy Observatory is operated by Associated Universities, Inc., under contract with the National Science Foundation. A few radio maps have been obtained from the Merlin archive. The work at SAO is supported by NASA-GRANT GO1-12125A and the work at RIT was supported by *Chandra* grant GO8-9114C. F. Massaro acknowledges the Foundation BLANCEFLOR Boncompagni-Ludovisi, n'ee Bildt for the grant awarded him in 2009 and in 2010. This work is supported in part by the Radcliffe Institute for Advanced Study at Harvard University. G.R.T. acknowledges support from a European Southern Observatory (ESO) Fellowship partially funded by the European Community's Seventh Framework Programme (/FP7/2007-2013/) under grant agreement No. 229517.

Facilities: VLA, *CXO* (ACIS)

APPENDIX

IMAGES OF THE SOURCES

Although for many of our sources the X-ray data are comprised of rather few counts, we show here the radio morphology via contour diagrams which are superposed on X-ray event files that have been smoothed with a Gaussian. In Figures 7–32, the FWHM of the Gaussian smoothing function is given in the figure captions. When there is sufficient signal-to-noise ratio of the X-ray image to provide spatial information, we have added contours (cyan or white), which are normally separated by factors of two. Most of the overlaid radio contours increase by factors of four. The X-ray event files shown are in units of counts pixel^{-1} in the 0.5–7 keV energy range. The primary reason that figures appear so different from each other is the wide range in angular size of the radio sources.

REFERENCES

Appenzeller, I., Thiering, I., Zickgraf, F.-J., et al. 1998, ApJS, 117, 319
Arnaud, K. A. 1996, in ASP Conf. Ser. 101, Astronomical Data Analysis Software and Systems V, ed. G. Jacoby & J. Barnes (San Francisco, CA: ASP), 17

[20] http://www.jb.man.ac.uk/atlas/

Baum, S. A., Heckman, T. M., Bridle, A., van Breugel, W. J. M., & Miley, G. K. 1988, ApJS, 68, 643
Balmaverde, B., Capetti, A., Grandi, P., et al. 2012, A&A, 545A, 143
Buttiglione, S., Capetti, A., Celotti, A., et al. 2009, A&A, 495, 1033
Capetti, A., Trussoni, E., Celotti, A., Feretti, L., & Chiaberge, M. 2000, MNRAS, 318, 493
Carleton, N. P., Willner, S. P., Rudy, R. J., & Tokunaga, A. T. 1984, ApJ, 284, 523
Cash, W. 1979, ApJ, 228, 939
Cheung, C. C. 2007, AJ, 133, 2097
Chiaberge, M., Capetti, A., & Celotti, A. 2002, A&A, 394, 791
Davis, J. E. 2001, ApJ, 562, 575
de Koff, S., Baum, S. A., Sparks, W. B., et al. 1996, ApJS, 107, 621
Dunkley, J., Komatsu, E., Nolta, M. R., et al. 2009, ApJS, 180, 306
Fanaroff, B. L., & Riley, J. M. 1974, MNRAS, 167, P31
Fanti, C., Fanti, R., de Ruiter, H. R., & Parma, P. 1987, A&AS, 69, 57
Feretti, L., Dallacasa, D., Govoni, F., et al. 1999, A&A, 344, 472
Floyd, D. J., Axon, D., Baum, S., et al. 2008, ApJS, 177, 148
Freeman, P., Doe, S., & Siemiginowska, A. 2001, Proc. SPIE, 4477, 76
Fu, H., & Stockton, A. 2008, ApJ, 677, 79
Giovannini, G., Cotton, W. D., Feretti, L., Lara, L., & Venturi, T. 2001, ApJ, 552, 508
Gopal-Krishna, & Wiita, P. J. 2000, A&A, 363, 507
Hardcastle, M. J., Evans, D. A., & Croston, J. H. 2009, MNRAS, 396, 1929
Harris, D. E., Massaro, F., & Cheung, C. C. 2011, http://www.oa.uj.edu.pl/jets2011/index.html
Harvanek, M., & Hardcastle, M. J. 1998, ApJS, 119, 25
Kalberla, P. M. W., Burton, W. B., Hartmann, D., et al. 2005, A&A, 440, 775
Kharb, P., Lister, M. L., & Cooper, N. J. 2010, ApJ, 710, 764
Kocevski, D. D., Ebeling, H., Mullis, C. R., & Tully, R. B. 2007, ApJ, 662, 224
Liuzzo, E., Giovannini, G., Giroletti, M., & Taylor, G. B. 2009, A&A, 505, 509
McCarthy, P. J., Spinrad, H., & van Breugel, W. 1995, ApJS, 99, 27
Mackay, C. D. 1971, MNRAS, 154, 209
Madrid, J. P., Chiaberge, M., Floyd, D., et al. 2006, ApJS, 164, 307
Massaro, F., Chiaberge, M., Grandi, P., et al. 2009a, ApJ, 692, L123
Massaro, F., Harris, D. E., & Cheung, C. C. 2011, ApJS, 197, 24
Massaro, F., Harris, D. E., Chiaberge, M., et al. 2009b, ApJ, 696, 980
Massaro, F., Harris, D. E., Tremblay, G. R., et al. 2010, ApJ, 714, 589
Morganti, R., Killeen, N. E. B., & Tadhunter, C. N. 1993, MNRAS, 263, 1023
Morganti, R., Oosterloo, T., & Tadhunter, C. N. 1999, A&AS, 140, 355
Owen, F. N., & Laing, R. A. 1989, MNRAS, 238, 357
Piconcelli, E., Bianchi, S., Miniutti, G., et al. 2008, A&A, 480, 671
Privon, G. C., O'Dea, C. P., Baum, S. A., et al. 2008, ApJS, 175, 423
Spangler, S. R., & Bridle, A. H. 1982, AJ, 87, 1270
Spinrad, H., Marr, J., Aguilar, L., & Djorgovski, S. 1985, PASP, 97, 932
Sun, M., et al. 2012, ApJ, submitted
Tadhunter, C., Dickson, R., Morganti, R., et al. 2002, MNRAS, 330, 977
Tremblay, G. R., Chiaberge, M., Sparks, W. B., et al. 2009, ApJS, 183, 278